POLITECNICO DI TORINO

Master's Degree in Nanotechnologies for ICTs

Master's Degree Thesis

Acoustic topological states on RF Piezo-Electric MEMS Technology and possible sensing applications

Supervisors

Prof. Matteo COCUZZA

Prof. Cristian CASSELLA

Candidate

Niccolò SCALISE PANTUSO

April 2025

Summary

Since the discovery of the Quantum Hall effect and, consequently, the topological states, the interest for devices exploiting this kind of phenomena has grown significantly. These types of state are characterized by a surprising energy localization resulting in a high-quality factor. In the first part of this work, some possible topologies presented can be used to induce the creation of edge and corner states. With FEM simulations, in particular COMSOL, the dispersion relations of the single cells and supercells have been studied both in 2D and 3D. The topological states have been induced because of the breaking of the symmetry in specific directions. To prove the existence of the topological state, the Berry curvature has been calculated. The Berry curvature is a parameter directly linked to the topological nature of the states in a 3D system. In the second part of this work, some possible layouts are shown to convert the topological state into an electric signal. To perform this,SiO_2 periodic structures have been deposited on top of a piezo-electric material (AlScN) which can convert the RF mechanical signal into a RF electronic signal in the tens of MHz range. This kind of signal could be used as a sensor for various parameters, such as: acceleration, stress, vibration, temperature and even infrared.

Acknowledgements

I want to say thank you to everybody. Thank you to my old friends in Italy with whom I shared laughs and tears; Thank you to my new friends that accepted me and made me feel at home, even if I was on the other side of the World. Thank you to my family who followed and supported me during all these years. Thanks to my grandparents that inspired me and proved to me that it's always worth to fight in life. Simply, thanks to everybody, in some cases words are not enough to describe how impactful and important you have been (and still are). The only real way that I have to show my gratitude is through my actions, and I hope that those will be enough, but in any case I will do my best.

Table of Contents

List of Figures

Chapter 1

Introduction

1.1 Basis of Crystallography

To understand topology, it is fundamental to have a clear idea about dispersion relations and periodicity conditions. The first logical step to do so is studying crystalline structure. To do this, some basic concepts are needed. First of all, crystals are systems where the atoms are arranged with a certain periodicity into a lattice. The basis of this lattice is the Bravais lattice, the whole crystal can be directly obtained by rigidly move the Bravais lattice. The atomic position can be written by using the Bravais lattice basis:

$$r_j = x_j a_1 + y_j a_2 + z_j a_3 \tag{1.1}$$

where x_j, y_j and z_j are integer numbers, while a_1, a_2 and a_3 are the basis vectors. The crystalline structure can be now moved to the reciprocal space. In this space, it's way more effective to look at the atoms distribution not directly through their position but by considering the Fourier transform of their position. To construct the reciprocal lattice we build its vectors using the formulas:

$$b_1 = 2\pi \frac{a_2 \times a_3}{a_1 \cdot a_2 \times a_3}; b_2 = 2\pi \frac{a_3 \times a_1}{a_1 \cdot a_2 \times a_3}; b_3 = 2\pi \frac{a_1 \times a_2}{a_1 \cdot a_2 \times a_3}; \tag{1.2}$$

where $b_i \cdot a_j = 2\pi\delta_{ij}$. The reciprocal lattice vector are:

$$\mathbf{G} = v_1 \mathbf{b_1} + v_2 \mathbf{b_2} + v_3 \mathbf{b_3} \tag{1.3}$$

The reciprocal lattice becomes extremely handy when dealing with diffraction. When an impinging wave gets diffracted from a certain infinitesimal volume element it undergoes a phase shift. This phase shift can be described by a phase factor $e^{i(k-k')\cdot r}$, where $\mathbf{r}$ is the distance of the infinitesimal volume from the origin. When

$k - k' = -\Delta k = -G$ the diffracted has the same frequency of the impinging wave. This is called **Diffraction condition** and can be with the form:

$$\mathbf{k} \cdot (\frac{1}{2}\mathbf{G}) = (\frac{1}{2}\mathbf{G})^2 \tag{1.4}$$

Thanks to this definition, a reciprocal space can be defined. This space, called Brillouin zone, shows all the wave-vectors k which can undergo a Bragg reflection by the crystal. The Brillouin zone is the Weigner-Seitz cell in the reciprocal lattice, where the Weigner-Seitz cell is defined as: *the locus of points in space that are closer to that lattice point than to any of the other lattice points.*

1.2 Introduction to Phononic Crystals and Acoustic Metamaterials

To obtain topological effects in acoustic structures is fundamental to use metamaterials and phononic crystalls. The metamaterials are materials that, thanks to a certain level of engineerization, have new properties that are not present naturally. The first study of acoustic metamaterials and phononic crystals goes back to the early 90s, when Sigalas and Economou demonstrated the existence of band gaps in the phonon density of state and band structure of acoustic and elastic waves in three-dimensional structures. The basic functioning of phononic crystals can be reduced to a principle analogue to the Bragg scattering in photonics. Another significant discovery was the existence of localization phenomena due to the presence of defects. These defects (such as the absence of a row of rods in a periodic rods-array) can introduce available states in the band-gap generating a confinement of the waves and can be exploited to obtain structure such as waveguides.

1.2.1 One-dimensional Monoatomic Harmonic chain

The simplest example that can be taken into account to understand the functioning of phononic structures is the one-dimensional monoatomic harmonic crystal.

This structure can be modeled in a very simple but effective way using a chain of masses connected by springs (Figure:1.1). To make the model even simpler we can consider only the nearest-neighbor interactions and no external forces applied. The analytic form of the force over a single mass can be obtained directly:

$$m\frac{d^2u_j}{d^2t} = \beta(u_{j+1} - u_j) - \beta(u_j - u_{j-1}) \tag{1.5}$$

By assuming solutions of the form

$$u_n = Ae^{ikja}e^{i\omega t} \tag{1.6}$$

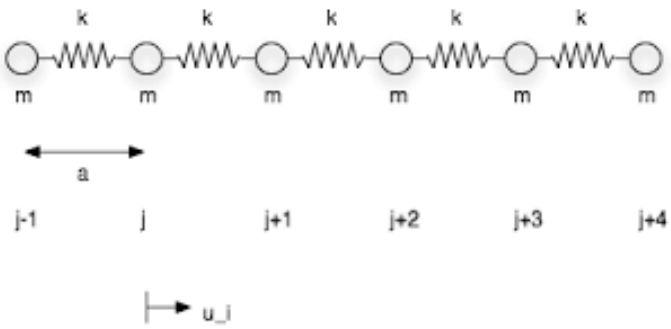

Figure 1.1: Mass spring model for a monoatomic one dimensional harmonic chain

which corresponds to propagating waves where k is the wave number and ω is the angular frequency, the equation 1.5 will have a solution of the form:

$$\omega(k) = \omega_0 sin(k\frac{a}{2}) \tag{1.7}$$

where $\omega_0 = 2\sqrt{\beta/m}$.

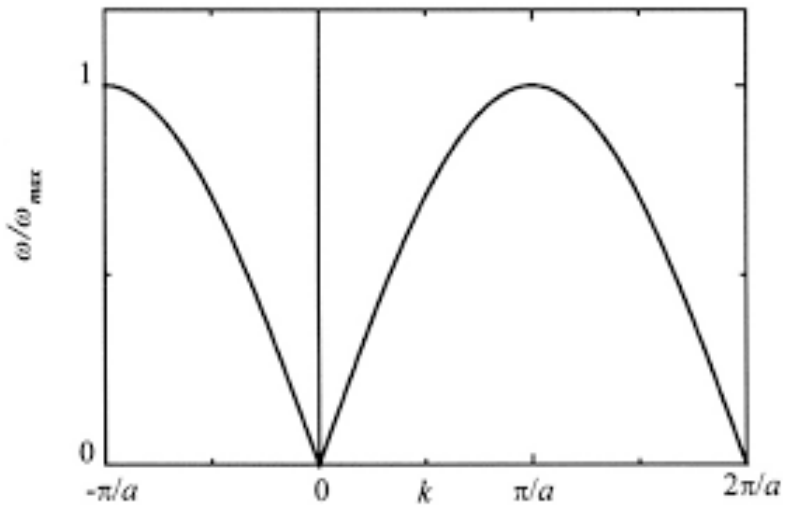

Figure 1.2: Band diagram of a 1D monoatomic harmonic chain

Now the band diagram of the 1D monoatomic harmonic chain can be plotted as we can see in Figure:1.2. From Figure1.2 and Equation1.7 we can see that the band diagram has a $2\pi/a$ periodicity, so we can focus our attention on the region between π/a and $-\pi/a$.

1.2.2 One-dimensional Diatomic Harmonic chain

In this paragraph is going to be analyzed a slightly more complex system with respect to the one in the previous paragraph. The focus is on a one dimensional diatomic harmonic chain of atoms.

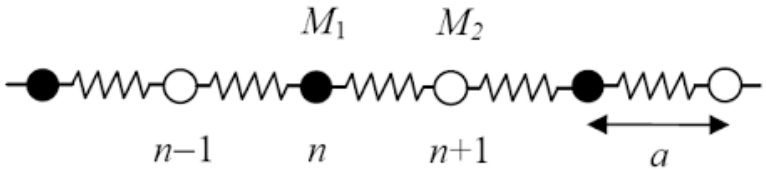

Figure 1.3: Mass spring model for a diatomic one dimensional chain

This new system is depicted in figure 1.3. Even in this case only the nearest neighbor interaction is considered. The motion of the system is described by a system of two equations of motion:

$$\begin{cases} m_1 u_n'' = \beta(u_{n+1} - u_n + u_{n-1} \\ m_2 u_{n+1}'' = \beta(u_{n+2} - u_{n+1} - u_n) \end{cases} \tag{1.8}$$

And can be assumed a solution of the form:

$$\begin{cases} u_n = Ae^{i\omega t}e^{ikna} \\ u_n = Be^{i\omega t}e^{ikn(a+1)} \end{cases} \tag{1.9}$$

As can be seen from equation 1.9, waves have different amplitudes for different masses. The only non trivial solution of this system can be obtained by setting to 0 the determinant of the following matrix:

$$\begin{vmatrix} 2\beta - m_1\omega^2 & -2\beta cos(ka) \\ -2\beta cos(ka) & 2\beta - m_2\omega^2 \end{vmatrix} = 0$$

From the last equation, two possible solutions can be obtained:

$$\omega^2 = \beta(\frac{1}{m_1} + \frac{1}{m_2}) \pm \sqrt{\beta^2(\frac{1}{m_1} + \frac{1}{m_2})^2 - 4\frac{\beta^2}{m_1 m_2} sin^2(ka)} \tag{1.10}$$

These solutions lead to a band diagram slightly different form the monoatomic case.

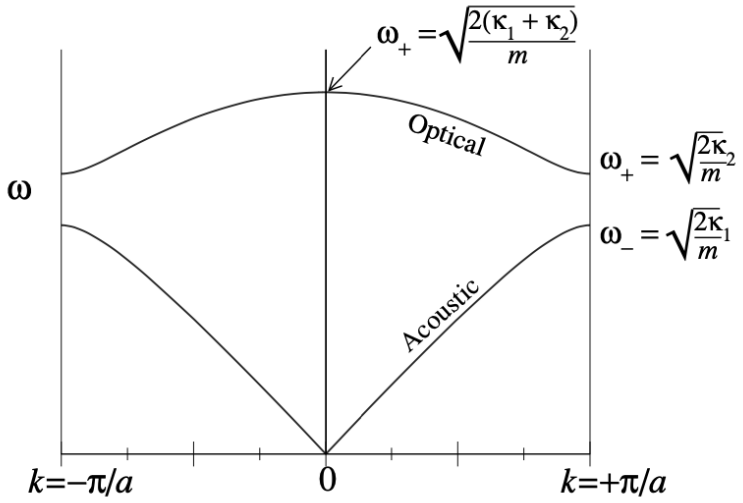

Figure 1.4: Dispersion relation of a diatomic harmonic chain

As can be observed in figure 1.4, the diatomic chain dispersion relation presents a band gap. This is due to the presence of two different masses inside the chain. In fact, if the masses were the same the dispersion relation would have had the same form of the monoatomic case.

1.2.3 Resonance in the presence of a side branch

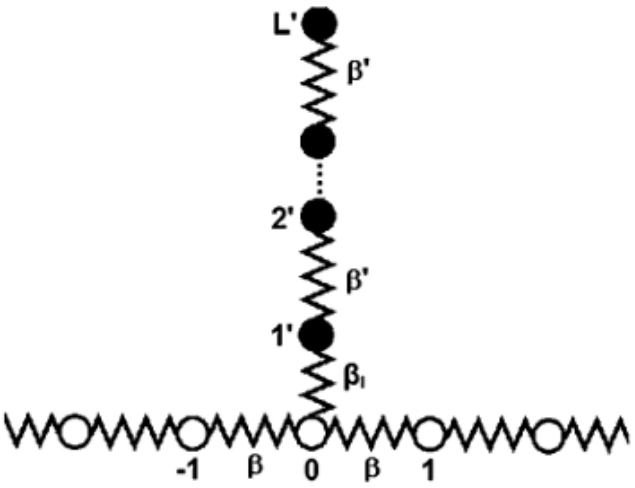

Figure 1.5: In the figure is depicted a system consisting in a monoatomic infinite chain with a side branch in a specific position

When a side branch is present,as shown in figure 1.5 the resonating phenomena become more complex to treat. The presence of the side branch complicates the equations of motion in the side branch, which take the form:

$$\begin{cases} -m'\omega^2 u_{n'} = \beta'(u_{n'+1} - 2u_{n'} + u_{n'-1}) for n' \neq 1', L' \\ m'\omega^2 u_{L'} = -\beta'(u_{L'} - u_{L'-1)} \\ m'\omega^2 u_{n'} = -\beta_I(u_{1'} - u_0) + \beta'(u_{2'} - u_{1'}) \end{cases} \tag{1.11}$$

In the site where the branch is connected the equation of motion will be:

$$-m\omega^2 u_0 = \beta(u_1 - 2u_0 + u_{-1}) + \beta_I(u_{1'} - u_0) \tag{1.12}$$

The general solution of the system described in equations 1.11 and 1.12 will be of the form

$$u_{n'} = A' e^{ik'n'a} + B' e^{-ikn'a'} \tag{1.13}$$

Putting this solution in equation 1.11 gives:

$$m_0\omega^2 = 2\beta'(1 - \cos k'a). \tag{1.14}$$

Subtracting 1.14 and 1.11 gives:

$$\beta'(u_{L'+1} - u_{L'}) = 0. \tag{1.15}$$

This equation serves as a boundary condition on site N' in the side branch. The displacement u_{L0+1}, at a fictive site $L0+1$, is a support for the boundary condition 1.15. Similarly, by subtracting the equation of motion 1.11 and that of the fictive site 1 the following boundary condition is obtained:

$$-\beta_I(u_{1'} - u_0) + \beta'(u_{1'} - u_{0'}) = 0. \tag{1.16}$$

The two boundary conditions at sites 1' and L' form the set of equations are:

$$u_{L'} - u_{L'+1} = 0, \tag{1.17}$$
$$(\beta_I - \beta')u_{1'} + \beta' u_{0'} = 0. \tag{1.18}$$

We insert the general solution 1.13 into 1.18 and obtain the set of linear equations:

$$A'e^{ik'L'a}(1 - e^{ik'a}) + B'e^{-ik'a}(1 - e^{-ik'a}) = 0, \tag{1.19}$$
$$A'(\beta_I - \beta')e^{ik'a} + \beta' + B'(\beta_I - \beta')e^{-ik'a} + \beta' = \beta_I u_0. \textbf{??} \tag{1.20}$$

Solving these equations gives the following:

$$A' = \frac{-\beta_I u_0 e^{-ik'L'a}(1 - e^{-ik'a})}{\Delta}, \tag{1.21}$$
$$B = \frac{\beta_I u_0 e^{ik'L'a}(1 - e^{ik'a})}{\Delta}, \tag{1.22}$$

where:

$$\Delta = -4i \sin\frac{k'a}{2}\left[(\beta_I - \beta')\cos\left(k'\left(L' - \frac{1}{2}\right)a\right) + \beta'\cos\left(k'\left(L' + \frac{1}{2}\right)a\right)\right]. \tag{1.23}$$

Finally, to find the perturbation V, we use 1.34 and 1.13 to obtain:

$$V(\omega) = \frac{2\beta'\beta_I \sin\frac{k'a}{2}\sin L'k'a}{(\beta_I - \beta')\cos k'\left(L' - \frac{1}{2}\right)a + \beta'\cos k'\left(L' + \frac{1}{2}\right)a}. \tag{1.24}$$

The effect of the side branch on wave propagation along the infinite crystal is understood more easily by considering the limiting case where $b = bI = b_0$ and $m = m'$ such that $k = k'$. Then, equation **??** simplifies to:

$$V(\omega) = \frac{2b \sin \frac{ka}{2} \sin L_0 ka}{\cos k\left(L_0 + \frac{1}{2}\right) a}. \tag{1.25}$$

At the standing wave frequency of the side branch, $V = 0$, corresponding to a full transmission state. The zeros of transmission scale with the number of atoms in the side branch, altering the band structure. The formalism required to analyze this further is based on the Green's function approach known as Interface Response Theory.

1.3 Topological Band theory

1.3.1 Quantum Hall effect

The topological study of matter started, and intensified, during the last 30 years, after the discovery of the Quantum Hall effect. The quantum Hall effect is a quantized version of the Hall effect that takes place in a 2D finite structure when a strong magnetic field is applied.

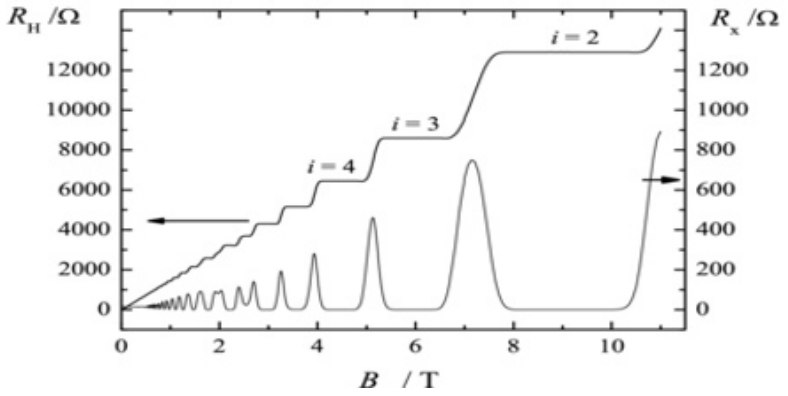

Figure 1.6: Resistance variation along the x axis when different magnetic field values are applied

In such a system, the Hall resistance R_{xy} is a step function.

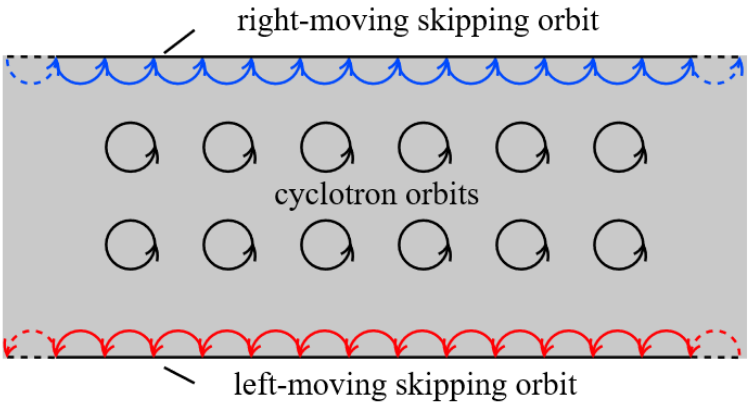

Figure 1.7: Electrons movement in the Quantum Hall effect

This is due to the topology of the system. By looking at figure 1.7, can be seen how the electrons on the edge can't maintain the orbit caused by the applied magnetic field, and are forced to move along the edge. In the picture, it can be observed that the electrons on the two edges will move in opposite directions, maintaining a zero net current. This discovery opened the way to the topological study of matter.

1.3.2 Concept of topology

Topology is an area of mathematics that investigates continuity and other related concepts.

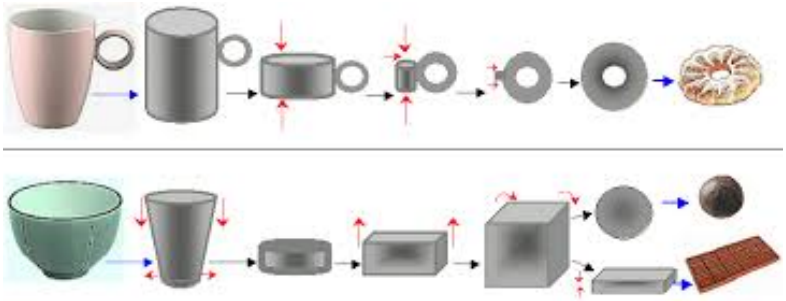

Figure 1.8: In the picture is shown how different objects are topologically equivalent

Figure 1.8 helps having a basic understanding of this definition. The presence of a hole in a torus makes it impossible to deform it into a sphere and vice versa. This implies that the sphere and the torus are in different topological classes. On the other hand, it can be noticed that a sphere can be deformed, by a continuous

transformation, into a cube. This is due to the presence of a hole in the torus that can't be created by simply deforming the sphere.

1.3.3 Spatial and time reversal symmetry

The next step is extending these concepts and their mathematical formulation over Quantum systems. To perform such a task, three basic concepts are needed:Dirac points, spatial and the time reversal symmetry.

The Dirac points are high symmetry points in the band diagrams. In this high symmetry points, conduction and valence band touch each other causing the closure of the band gap. When this happens, a degenerate cone-like dispersion is created.

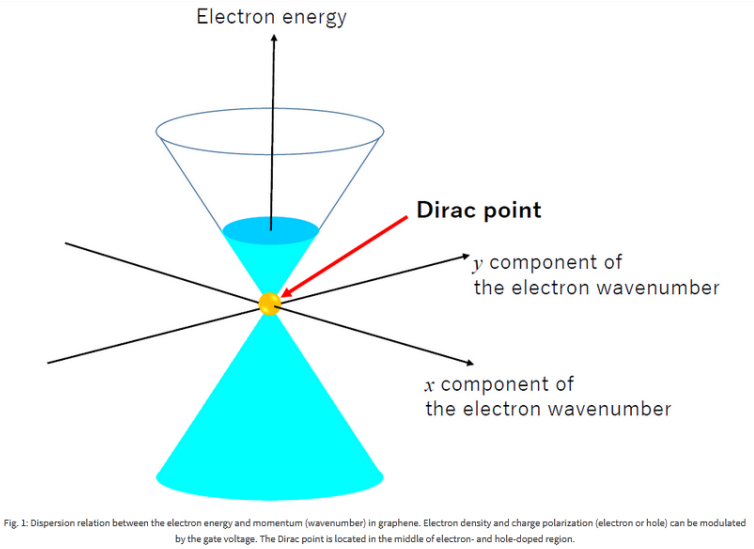

Figure 1.9: In the picture is shown a band diagram having a Dirac Point

This type of points are protected by spatial and time reversal symmetry, so to open a band gap is necessary to brake one of these symmetries.

These symmetries express the concept that, going from A to B or from B to A, either in a temporal or a spatial framework, produces the same output.The space reversal symmetry can be described through the σ operator. Such operator acts on the Hamiltonian in the following way:

$$\sigma H(k)\sigma = -H(k) \tag{1.26}$$

This symmetry, on the other hand, has been extensively treated in quantum physics and in the topological study of matter. As is discussed in [10], the time reversal symmetry is based on the operator Θ. Considered a periodic Hemiltonian

$H(t+T) = H(t)$ the time reversal operator act as:

$$H(-t) = \Theta H(t) \Theta^{-1} \tag{1.27}$$

If the condition H(t)=H(-t) holds then the time reversal symmetry is valid. It is even more interesting to notice what happens when this symmetry is broken. As an example of this second part, the Haldane analyses over graphene honeycomb is extremely explicative.

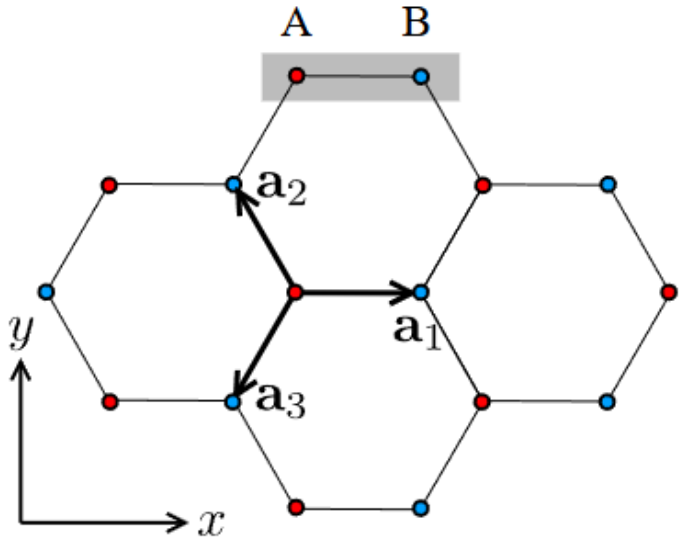

Figure 1.10: Here is show the 2D graphene structure

Haldene performed a study and characterization over graphene to make it topological. The graphene shows both sublattice spatial symmetry and time reversal symmetry. To brake the first one that can be assigned opposite on-site energy M or $-M$ to the A or B sites respectively. The Hamiltonian is then given by

$$H_0(\mathbf{k}) + M\sigma_z. \tag{1.28}$$

This leads to a gapped spectrum.

$$E(\mathbf{k}) = \pm\sqrt{|\mathbf{h}(\mathbf{k})|^2 + M^2}, \tag{1.29}$$

As can be observed in equation 1.29, by braking this symmetry we create two distinct gapped states. But, it's a not very interesting and basic case due to the

fact that the states will be simply localized either on state A or on state B. On the contrary, is way more interesting to study the braking of the time reversal symmetry.

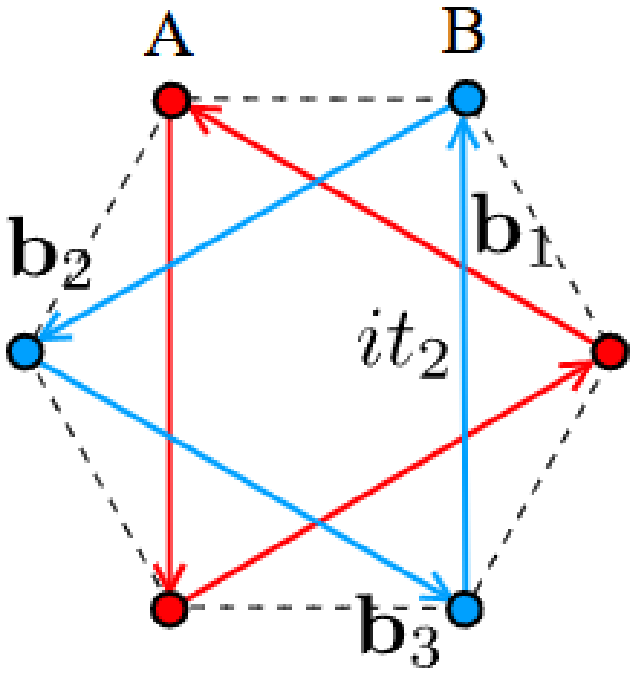

Figure 1.11: Here is show the Haldene model for the time reversal symmetry braking in the graphene structure

A way to brake the symmetry is by introducing a imaginary second-nearest neighbor hopping, with the pattern showed in figure 1.11, where the directions of the arrows denotes the two opposite hopping directions. By doing so the Hemiltonian becomes:

$$H(\mathbf{k}) = H_0(\mathbf{k}) + M\sigma_z + 2t_2 \sum_i \sigma_z \sin(\mathbf{k} \cdot \mathbf{b}_i) \tag{1.30}$$

When t_2 overcomes a value $\pm M/3\sqrt{3}$, the gap closes and changes sign.

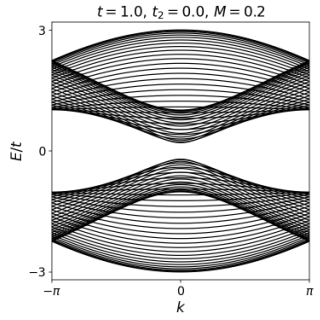

(a) Band diagram for the graphene when $t_2 < \pm M/3\sqrt{3}$

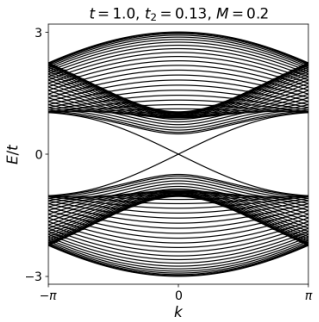

(b) Band diagram for the graphene when $t_2 > \pm M/3\sqrt{3}$

Figure 1.12: In the figure is shown how an edge state appear after $t_2 >$ overcomes $\pm M/3\sqrt{3}$

So there is an inversion in the bands at the Dirac point which leads to a topological edge state, this is shown in figure 1.12; this concept will be better explained in the following sections.

1.3.4 Berry Phase, Chern number and topological insulators

As said in the previous section, by braking spatial and temporal symmetry band gaps are generated. When this gaps arise, a topological insulator is obtained. In this kind of insulator the bulk behaves like a classic insulator while the surface will necessary have a gapless band diagram due to the inversions of the bands.

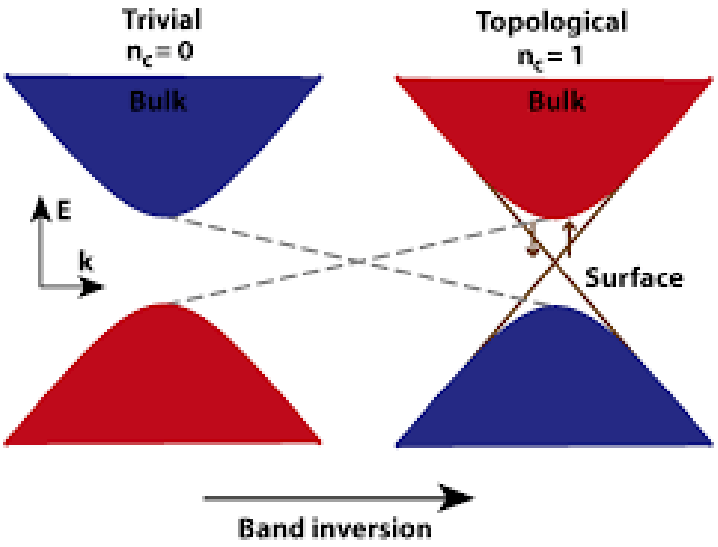

Figure 1.13: Comparison between trivial and topological insulator considering the band inversion

This inversion of the bands and the presence of a gapless band diagram on the surface is shown in figure 1.13. While deforming in an adiabatic way the bands of a system, certain fundamental properties (such as the quantized value of the Hall conductance, and the number of gapless boundary modes) cannot change unless the system passes through a quantum phase transition. In this way different groups of topological systems can be identified. In practice, a quantum phase transition is a transition that takes place when the bandgap of a certain system is closed (such as in the band inversion case). Strictly related to the concept of qunatum phase transition is the Berry phase. The Berry-phase is the phase acquired by the system while undergoing an adiabatic evolution along a closed path. The extremely interesting aspect of the Berry phase is that even if the evolution of a time-dipendent Hemiltonian is considered, the Berry-phase will be time independent and simply related to the closed path along which it is calculated (as long as the adiabatic condition is satisfied). This is expressed in the following equation:

$$|\Psi_n(t)\rangle = e^{i\gamma_n} e^{-\frac{i}{\hbar}\int_0^t dt' \varepsilon_n(\mathbf{R}(t'))} |n(\mathbf{R}(t))\rangle, \tag{1.31}$$

where the second exponential term is the "dynamic phase factor" and the first exponential term is the geometric term, with γ_n being the Berry phase. By requiring the state $|\Psi_n(t)\rangle$ to satisfiy the time-dependent Schrödinger equation, it can be shown that:

$$\gamma_n(t) = i\int_0^t dt' \langle n(\mathbf{R}(t'))|\frac{d}{dt'}|n(\mathbf{R}(t'))\rangle = i\int_{\mathbf{R}(0)}^{\mathbf{R}(t)} d\mathbf{R}\langle n(\mathbf{R})|\nabla_{\mathbf{R}}|n(\mathbf{R})\rangle, \quad (1.32)$$

The element $\langle n(\mathbf{R})|\nabla_{\mathbf{R}}|n(\mathbf{R})\rangle$ is called Berry connection, which describes how the eigen-states of the Hamiltonian change as the parameters $\mathbf{R}$ vary. This connection leads to the Berry curvature. From the Berry phase we can obtain the Chern number through equation:

$$C = \frac{1}{2\pi}\int_{\mathrm{BZ}} d^2k\, \Omega(\mathbf{k}) \quad (1.33)$$

where the Berry curvature $\Omega(\mathbf{k})$ is defined as:

$$\Omega(\mathbf{k}) = \nabla_{\mathbf{k}} \times \mathbf{A}(\mathbf{k}) \quad (1.34)$$

where A in equation 1.34 is the previously mentioned Berry connection.

A fundamental aspect of the Chern number is the fact that it is a topological invariant. In fact we can define a topological class of insulator as the group of insulators that have the same Chern number. It must be considered that by changing the Hamiltonian near the surface, the dispersion of the edge states is modified. Changing for instance the number of times that the Fermi energy will be crossed by some states. However, the difference $N_R - N_L$ between the number of right and left-moving modes cannot change and is determined by the topological structure of the bulk states. This is summarized by the bulk-boundary correspondence:

$$N_R - N_L = n. \quad (1.35)$$

where n is the Chern number.

Chapter 2

Topology applied to phononic structures

2.1 From quantum to phononic systems

The theory described in the previous chapters can be extended to other fields such as phononics and photonics. The main focus in this thesis will be on phononics systems. As explained in the introduction, even in a phononic system we can obtain a band diagram. This band diagram will come from the possible vibrational modes of a periodic system. Like in the quantum mechanical case, also this kind of band diagram can be deformed thanks to topology and can lead to different type of insulators. What has been previously said about the topological study of a quantum system is still holding, the biggest difference is that the main characters here are not electrons but quanta of vibration: phonons. The eigenstates will be the allowed resonance frequencies , and the eigenmodes will be the possible vibrational modes of the system.

Here are going to be analyzed different structures and how mass loading, physical parameters (such as Young's modulus and density) and geometrical parameters influence the dacoustic behavior of the system.

2.2 FEM simulations

To analyze the different structures, has been employed a finite element model (FEM). The numerical solutions have been obtained through COMSOL multiphysics, using the piezoelectric module. Thanks to this software a numerical solution of the coupled electrical-mechanical equations has been calculated. The COMSOL software has been employed for both eigen-studies and frequency studies. For what concerns

the eigen-states study, periodic boundary conditions have been imposed as Floquet boundary conditions. This conditions come from the Floquet theory, which treats a branch of the ordinary differential equation theory. In particular it involves periodic linear differential equation of the form:

$$\dot{f} = A(t)f \tag{2.1}$$

where $f \in R^n$ and $A(t) \in R^{n \times n}$ with period T. The COMSOL software solves two sets of equations, one for the frequency study and one for the eigen-study. The frequency study equations are:

$$\rho w^2 \mathbf{u} = \Delta \cdot (FS)^T + Fve^{j\phi}, F = I + \Delta \mathbf{u} \tag{2.2}$$

$$\Delta \cdot \mathbf{D} = \rho_v, \mathbf{E} = -\Delta V \tag{2.3}$$

While the eigen-study equations are:

$$\rho \omega^2 \mathbf{u} = \Delta \cdot (FS)^T, F = I + \Delta \mathbf{u}, -i\omega = \lambda \tag{2.4}$$

$$\Delta \cdot \mathbf{D} = \rho_v, \mathbf{E} = -\Delta V \tag{2.5}$$

2.3 First geometry: elliptical rods over AlScN substrate

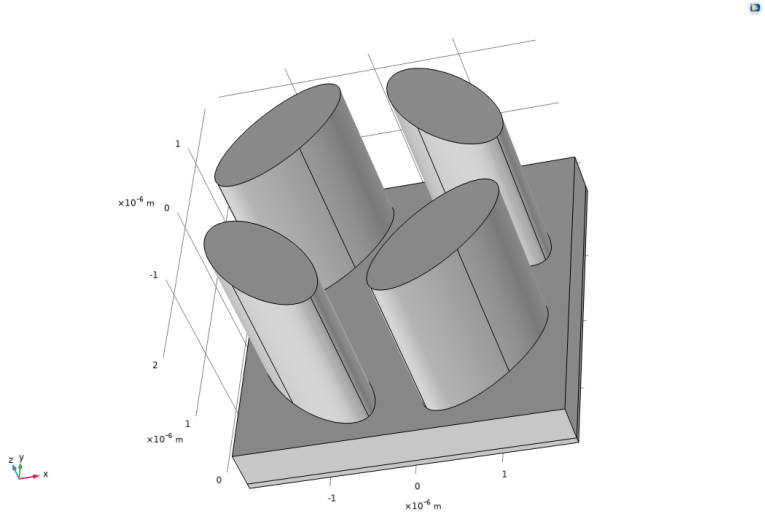

Figure 2.1: Unit cell consisting in a squared shaped bulk with elliptical rods on top of it

The first unit cell taken into account is the one depicted in figure 2.1. This unit cell is composed by a 500 nm thick $AlScN$ squared substrate with elliptical rods of SiO_2 on top of it. The rods height is $2.1\mu m$, while the edge of the single cell is $a = 3.8\mu m$. The cell presents also a $80nm$ platinum bottom layer that will be used as a ground when the cell is electrically driven. By tuning the shape, the rotation angle, the height of the rods we can directly influence the dispersion relation. This geometry was previously analyzed in [36], in that paper is studied a way larger geometry and the whole structure is made in $Si(100)$.

At first, the structure was scaled to reach micro-metric dimensions. After that the substrate was changed from $Si(100)$ to $AlScN$.

This substitution was performed to allow the possibility of having an electrical readout from the acoustic response of eventual devices based on this type of cell and technology. In Fact the AlScN is a piezoelectric material, a material able to convert strain into an electrical signal and vice versa

As shown in [36] paper, the rotation of the elliptical pillars causes the opening of a band gap around 0.9MHz, moreover, the rotation direction influences how the band gap opens. If the rotation direction is positive the cell behaves like a normal insulator. On the other hand, when applying a negative rotation angles, the system becomes a topological insulator. This can be proved by looking at the Berry phase in high symmetry points.

2.3.1 Opening of bandgaps and tuning of the band diagram

As in the quantum mechanical case, even here we can tune and deform the band diagram like in the case explained by Professor Haldane in [22]. This can be obtained by applying periodic structures with different bulk modulus E and different densities ρ. An example of this can observed by comparing figure 2.4a and figure 2.4b the phononic band diagram of a simple block of AlScN with an AlScN with some periodic structures on top of it.

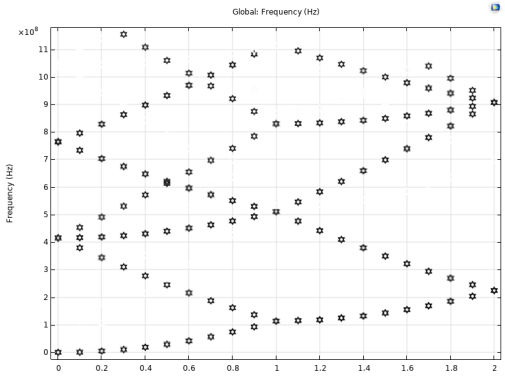

(a) simple Block of AlScN dispersion relation, no band gap is present

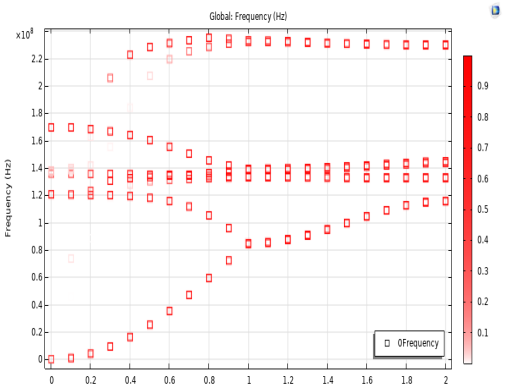

(b) Block of AlScN with with SiO_2 rods dispersion relation, a band gap opens above 120MHz

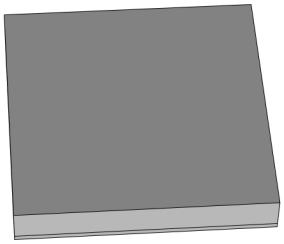

(c) Block of AlScN

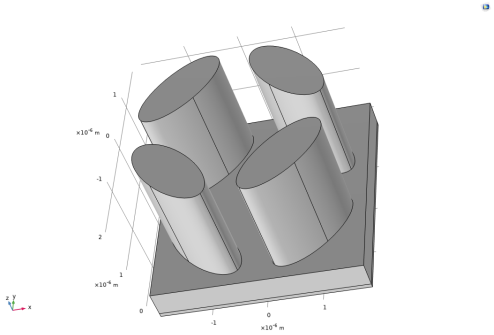

(d) Block of AlScN with SiO_2 rods

Figure 2.2: Main caption for the figure with subfigures

2.3.2 AlScN material characterization

Here is reported a brief introduction to the AlScN. Aluminum Scandium Nitride is a ternary compound formed by alloying Aluminum Nitride with Scandium. This material has garnered significant attention due to its enhanced piezoelectric properties compared to pure AlN. The addition of Scandium disrupts the crystal symmetry of AlN, leading to a substantial increase in piezoelectric coefficients, making AlScN highly suitable for applications in microelectromechanical systems (MEMS), radio frequency (RF) filters, and energy harvesting devices. AlScN also exhibits ferroelectric behavior at certain Sc concentrations (and for high voltages), opening avenues for non-volatile memory applications. It has a wide bandgap (6 eV) and high thermal stability. Which makes it an excellent candidate for high-power and high-temperature electronic devices. In terms of mechanical properties, AlScN

has a Young's modulus typically ranging between 220 and 400 GPa, depending on the Scandium concentration and the crystal orientation. This high stiffness is advantageous for MEMS applications, where mechanical robustness is crucial. Additionally, AlScN exhibits a high acoustic propagation velocity, generally around 6000 to 7000 m/s, which is beneficial for high-frequency acoustic wave devices such as surface acoustic wave (SAW) and bulk acoustic wave (BAW) resonators. These properties, combined with its superior piezoelectric performance, position AlScN as a versatile material for next-generation technologies. Although the AlScN exhibits a considerable acoustic velocity, this parameters its still lower than the SiO_2 deposited on top of it, whose longitudinal propagation velocity is around $11.85km/s$ and a transverse velocity of $6.12km/s$.

2.3.3 Band tuning

Theoretically, every geometric parameter will directly influence the wave propagation but, in this case, the bulk dimensions will be left unchanged, to facilitate manufacturability, and the tuning will be performed by changing the rod dimensions. The first goal is to open a band gap in the dispersion of the AlScN bulk. To obtain this effect elliptical rods are deposited on top of it, all rods will be rotated by a certain angle with respect to the Cartesian axis, assuming the x and y axes along the bulk edges. The rotation of the ellipses is fundamental to obtain the gap opening, in fact until one of the axis of the ellipses is parallel with respect to one of the edges of the substrate, no band gap will be opened.

2.3.4 Rotation angle

The first parameter that can be modified is indeed the rotation angle of the ellipses axes. This parameters, as has been shown by [36] causes a change in the size of the bandgap; with a maximum size reached around $\theta = 45°$. The rotation is a fundamental parameter to tune the topological index of the system.

2.3.5 Rods height

The rods height directly shift (almost linearly) the band gap. In fact the gaps are due to the fact that the rods will enter a resonance state absorbing the vibrations of the bulk and, as a consequence, blocking the wave propagation. In this view it's pretty straightforward to see that higher rods will have lower resonance frequencies and vice-versa.

2.3.6 Ellipses axis lenght and ratio

All the concept behind the gap opening revolves around the concept of performing a mass loading of the bulk with different materials. Changing the axis dimensions directly change the coverage of the pillars over the substrate modifying the mass loaded and the spring model system. Another important aspect is the aspect ratio of the rod. In fact, if cylindrical rods would have been employed the rods rotation would have not had any effect. This is pretty straightforward. As a consequence, it is logic to think that the more the cross section of the rods will be further from the a perfect circle, the more the rotation angle is going to be effective to tune the band gap opening.

2.3.7 Topological and normal insulator

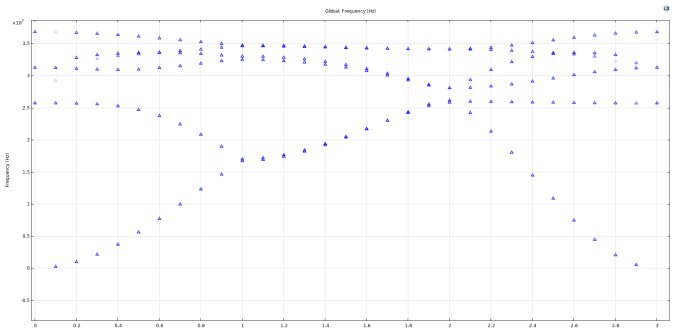

(a) Dispersion relation of a unit cell with rods rotated by $-45°$

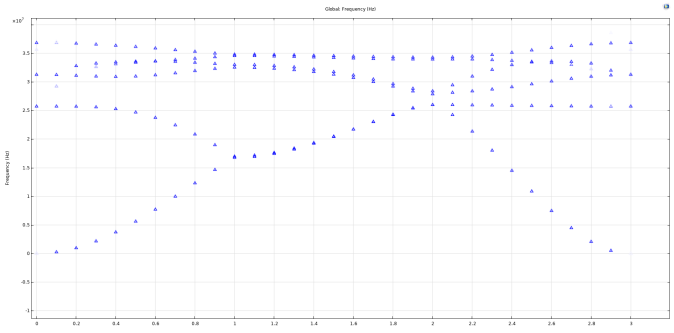

(b) Dispersion relation of a unit cell with rods rotated by $45°$

Figure 2.3: Here is shown a comparison between the dispersion relation of 2 different cell with opposite rotation angles,$-45°$ and $45°$

In figure 2.3 can be seen that by depositing rods with opposite orientations (specifically $-45°$ and $45°$)very similar dispersion relations are obtained. This is true from an eigenfrequency point of view.

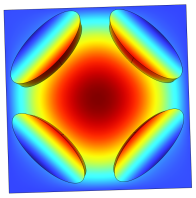

(a) Dispersion relation of a unit cell with rods rotated by $-45°$, k=2 and frequency=25MHz

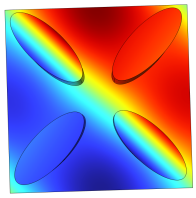

(b) Dispersion relation of a unit cell with rods rotated by $45°$, k=2 and frequency=25MHz

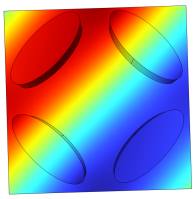

(c) Mode shaper of a unit cell with rods rotated by $-45°$, k=2 and frequency=28MHz

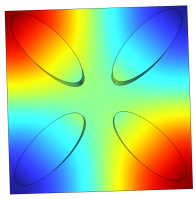

(d) Mode shaper of a unit cell with rods rotated by $45°$, k=2 and frequency=28MHz

Figure 2.4: Here it is shown a comparison between the modes of 2 different cell with opposite rotation angles, we can see that the mode shape is inverted

But the displacement modes, as can be observed in figure 2.4 will have inverted parity (a first sign that a band inversion took place) and different Chern numbers, which confirms the different topological nature of the two gaps. In particular, the insulator obtained thanks to the $45°$ rods is a trivial insulator, where no band inversion took place. On the other hand, the $-45°$ case is a higher-order topological insulator, in which the rods cause a band inversion and a consequent change in the Chern number.

2.3.8 Edge state

It is extremely interesting to observe what happens when insulators with different Chern numbers are linked together. Let's remind that in this case the Chern number variation is due to the Inversion of the bands described in figure 1.13 . A first extremely naive but effective consideration is that a sort of transition between the two band diagrams has to take place to have continuity. This transition generates

two allowed states called edge states. The edge states are localized at the interface between the trivial and the topological insulator. This edge states are in gap states that allow traveling waves along the interface. The two edge states have opposite group velocity, leading to opposite energy fluxes, due to this characteristic the two edge states are chiral states featuring backwards and forwards propagation.

2.3.9 Corner states

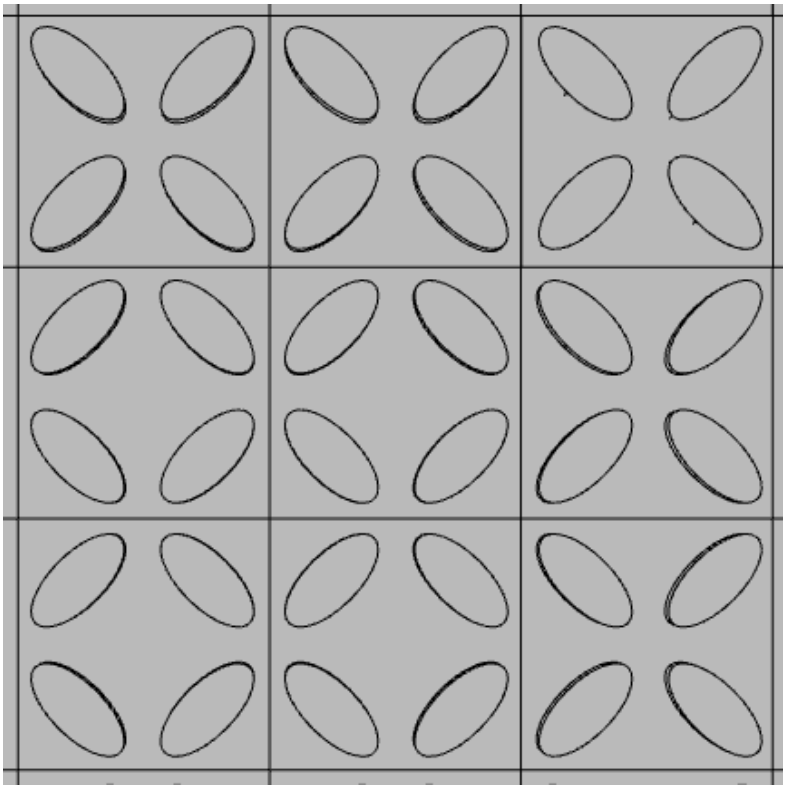

Figure 2.5: Corner formed by the intersection between two interfaces, one along x and the other along y

By looking at the edge states, a question that can come to mind could be: What would happen if there were interfaces along multiple direction, such as figure 2.5. The concept that was applied to justify the existence of edge states can be directly extended to corners. In fact the braking of the symmetry along two different directions causes the generation of a corner states. In this kind of topological state the energy is confined in a 0D space. A major difference with respect with the edge states is that the corner states are stationary states, where there isn't a net flux of energy in any direction. An interesting point about the corner state, is that their

dispersion relation is a flat line in the middle between the two edge state dispersion curves, so the corner states are characterized by 0 velocity group. In fact, in the corner states is localized stationary energy, in contrast to the edge states where the energy is chiral and so it propagates along the interface.

2.4 Second geometry: SSH cell

The second type of geometry considered in this work is the Su-Schrieffer-Heeger (SSH) cell. The SSH model, originally proposed to describe the electronic structure of poly-acetylene. At its core, the SSH model describes a chain of dimerized atoms, where alternating strong and weak hopping amplitudes between neighboring sites give rise to a band structure with distinct topological features.This model can be used to explain and describe a two-dimensional topological acoustic insulator. Like the previous case, here a specific symmetry is broken to open a band gap.

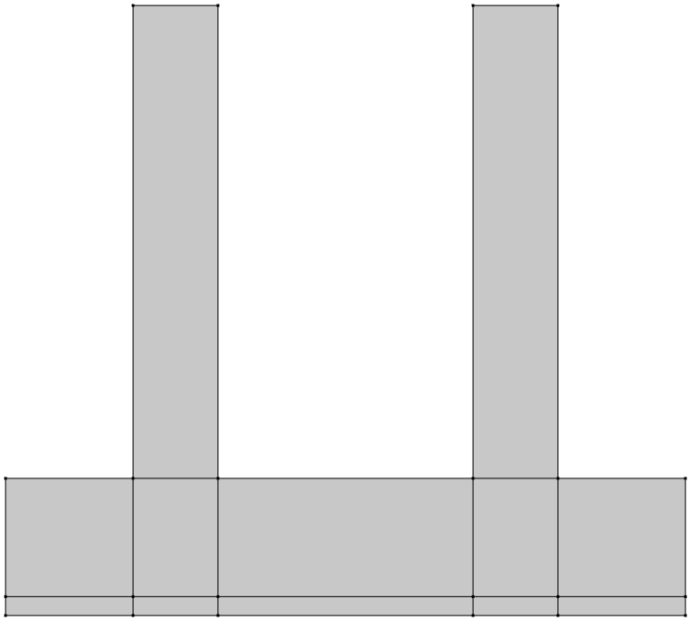

Figure 2.6: SSH A0 cell

In this case the geometry of the cell is quite simple, as described in figure 2.6 the unit cell is constituted by an AlScN substrate with two rods of SiO_2 deposited on top of it. The starting unit cell that is going to be described here has a $24\mu m$ wide and $0.5\mu m$ thick substrate, while the rods are $3\mu m$ wide and $2\mu m$ thick. This structure has been deeply studied in the paper [8]. The band diagram of the

above structure will be tuned and studied by changing the rods dimensions and the distance between the two rods. In the previous case the band gap was created thanks to the inversion of the bands and the "breaking" of the Dirac point. Here, the band gap is opened through a different mechanism. The presence of the rods causes a coupling between higher order modes, in particular an higher order S mode is coupled with the A_0 mode. This coupling is possible because the higher order modes are not purely longitudinal or transverse, and so the higher order S modes can interact with the A_0 mode.

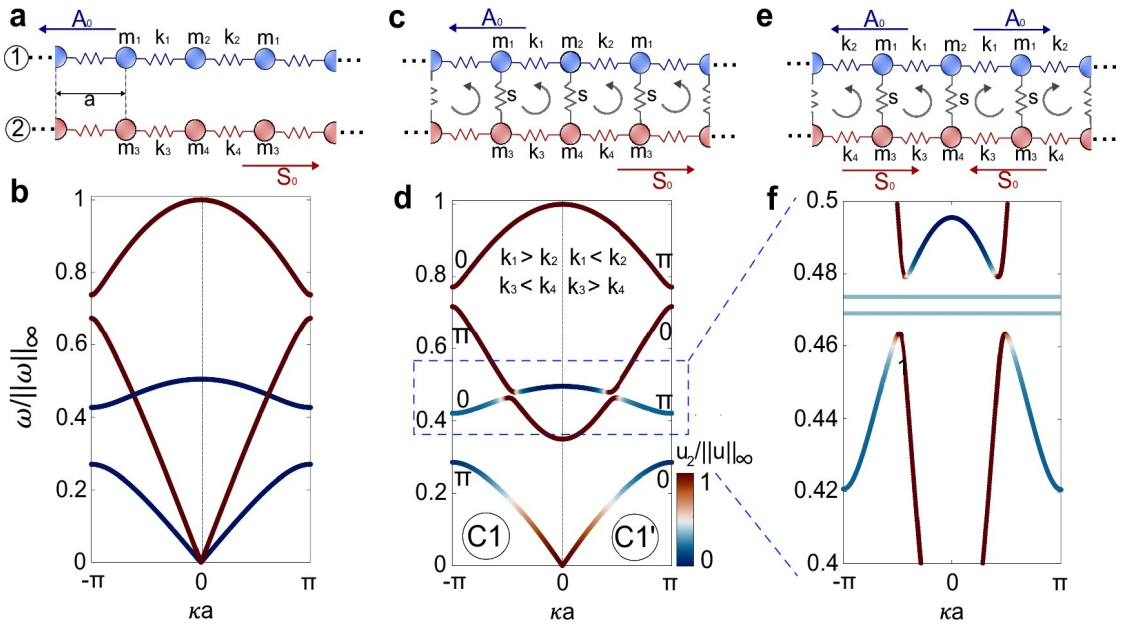

Figure 2.7: Spring model for A0 A1 cell and the supercell structure, showing also two edge states.

This behavior is depicted in figure 2.7 where a the system is framed through a mass spring model. In this simple model, the coupling is introduced by using springs which connect the two chains. In the figure the coupling takes place between the two fundamental modes A0 and S0 because it is enforced by the s springs. In a real and more complete model, the coupling between fundamental modes doesn't take place because these modes are respectively purely transversal and purely longitudinal.

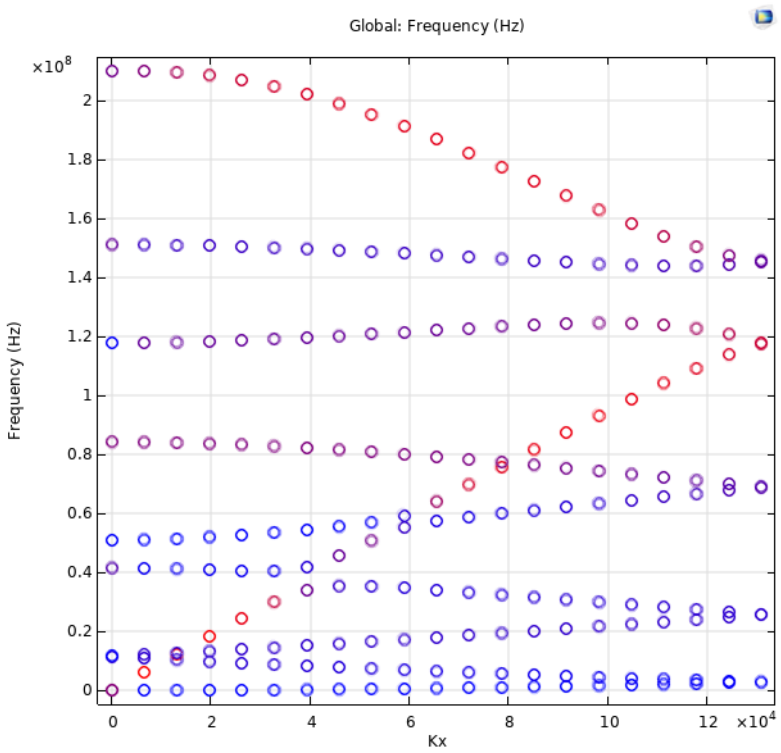

Figure 2.8: SSH dispersion relation of a unit cell where the symmetry is not broken (Cell A0), can be observed how the coupling here is almost non existing and a Dirac Point is present around 80MHz

This can be shown easily by using a FEM, both the single cells and the supercells have been studied in COMSOL and with a Matlab script to obtain displacement and dispersion relations, such as the one in figure 2.8.

2.4.1 Bandgap opening and dispersion relation tuning

The tuning of the rods displacement is a fundamental procedure to induce the opening of band gaps. In figure 2.8 is show the dispersion relation of the A0 cell, in this cell the distance between the rods and the center of the cell is equal to the distance between the rods and the edge of the cell. In this dispersion relation has been used a color scale to highlight the nature of the mode, transverse modes are characterized by the blue color while longitudinal modes are depicted in red. It is interesting to see that for modes above the fundamental one it is possible to obtain a coupling between transverse and longitudinal modes; in fact these coupling regions have a more purple color (for example, the band gap that opens near 40 MHz). The coupling between longitudinal and transverse modes is possible thanks to the fact that higher order modes are neither purely transverse or purely longitudinal

but have both components. Another very interesting point in the above mentioned dispersion relation is the crossing point between the first longitudinal mode and the sixth transverse mode, around 80 MHz. Although the sixth transverse mode is far from being purely transverse, there is no coupling with the fundamental longitudinal mode. This suggests that by some sort of tuning and by breaking the symmetry of the cell should be possible to open a considerable band gap in that region. To do so, a tuning of the position of the rods is performed. In the A0 cell the distance between the center of the cell and the rod was $4.5\mu m$ and it was equal to the distance between the rod and the edge of the cell. The rods can be moved either towards the center or towards the edges of the cell, by this translation two different types of cell can be obtained: A1 and A2. Cell A1 has a distance between rods and center of $2\mu m$ while in cell A2 the rods are $2\mu m$ distant from the edges.

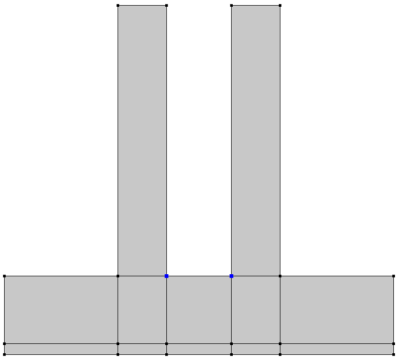

(a) SSH A1 cell geometry with $t_{AlScN} = 500nm$and $t_{SiO_2} = 2\mu m$,with a width of and a distance between the rods of $4\mu m$

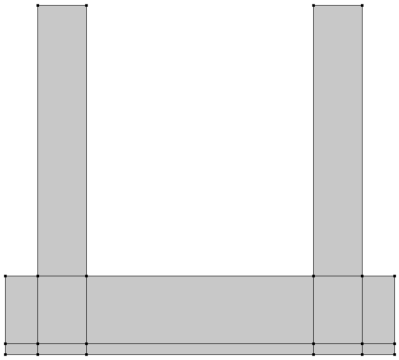

(b) SSH A2 cell geometry with $t_{AlScN} = 500nm$ and $t_{SiO_2} = 2\mu m$, and a distance between the rods of $14\mu m$

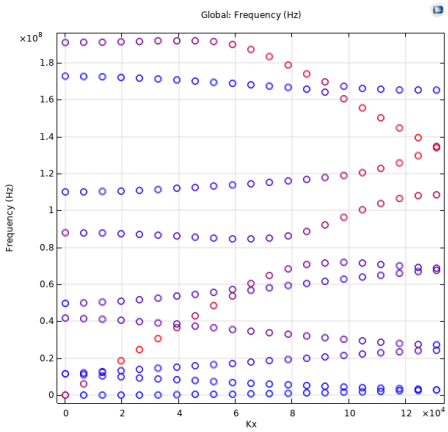

(c) SSH A1 cell dispersion relation

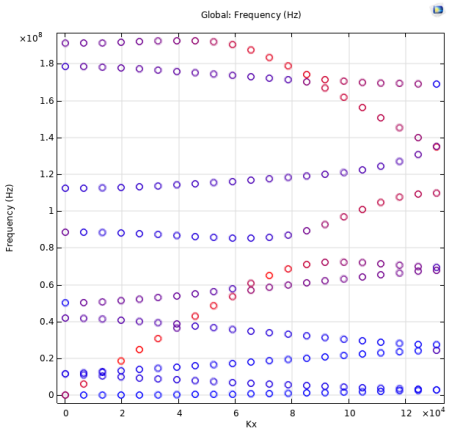

(d) SSH A2 cell dispersion relation

Figure 2.9: Disperion relation of A1 and A2 cell with the correspective geometries

By applying this displacement the dispersion relation deeply changes. In figure 2.9d and figure 2.9c are shown the dispersion relations of A2 and A1 cell respectively. Although the dispersions relations seem identical there is a considerable difference in the mode shapes around the band gap.

(a) Mode shape A1 cell 70Mhz

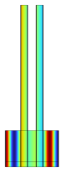

(b) Mode shape A1 cell 90Mhz

(c) Mode shape A2 cell 70MHz

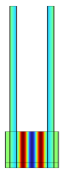

(d) Mode shape A2 cell 90Mhz

Figure 2.10: Mode shape for cell A1 and A2 for the states at the edges of the bandgap

As can be seen in fig 2.10 the parity of the modes for the two types of cell is inverted. Can be observed that the cell A1 mode will be even at 70 MHz while cell A2 mode is going to be odd at the same frequency, the behavior it's inverted for modes at the next eigenfrequency (90 MHz) . This difference is due to the opposite type of translation that has been performed. And can be seen as a proof of the topological change between the two structures.

2.4.2 Tuning band gap

Rods height

The first parameter that can be used to tune the dispersion relation is the thickness of the rods. The thickness directly affects the resonant frequency of the rods. Thicker rods will lead to lower resonant frequency while thinner rods will have a higher resonant frequency. From this we can foresee that changing the rod thickness will cause a shift in the dispersion relation frequency of the system (towards upper frequencies for thinner rods and towards lower frequencies for thicker rods). It is also important to take in consideration the mass loading effect of the rods, which is one of the main characters in the deformation of the band diagram.

Rods width

As just said, one of the main actors that allows the band tuning is the mass loading performed by adding the periodic structures on top of the bulk, so can be understood straightforwardly that changing the width of the rods will directly affect the amount of mass "loaded" on top of the bulk. This different loading can be used to tune the coupling between transverse and longitudinal modes and directly change the band gap dimensions. Also if the device is not properly scaled with the width of the rods, the periodicity of the structure is altered and this has huge effects on its topological behavior.

2.4.3 Edge states

Even in this case, like the one described in section 2.3.8, the most interesting case of study is when cells having different Chern numbers and, as a consequence, different mode parity, are juxtaposed. In this paragraph cell A1 and A2 are going to be used as an example.

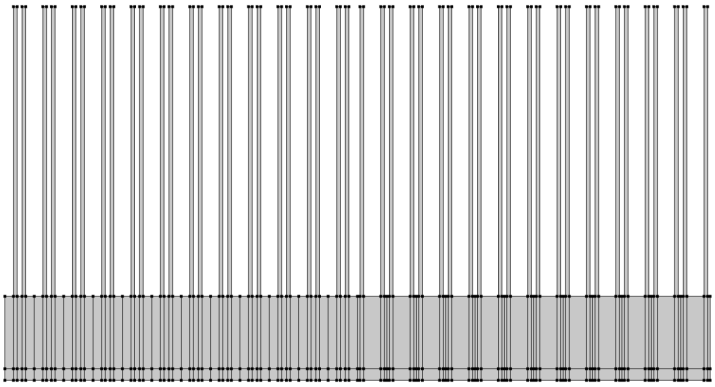

Figure 2.11: SSH supercell structure

The edge state is studied in a supercell built by linking one array of A1 cells with an array of A2 cells, as shown in 2.11. In this system, due to the fact that the two cells have different topological indexes, two edge states are created in the band-gap.

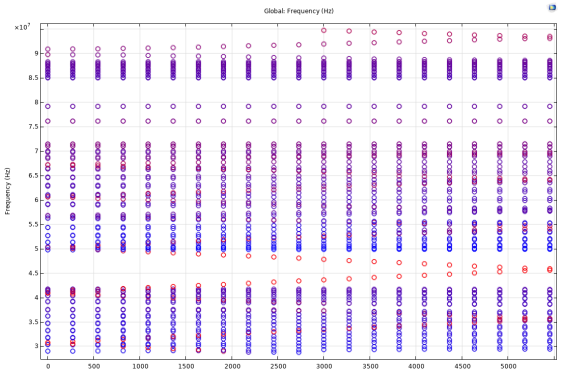

(a) SSH supercell dispersion

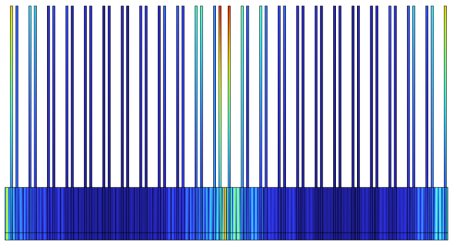

(b) First edge state displacement

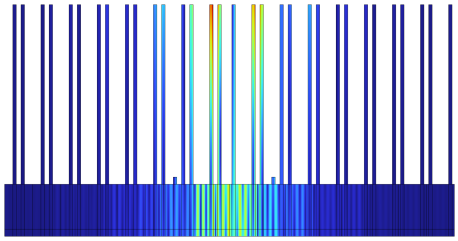

(c) Second edge state displacement

As can be observed in Figure 2.12b and Figure 2.12c, the edge states are localized at the interface between the A1 and the A2 array. This states shows a high robustness to defects. This is due to the topological nature of the localized states. In fact, defects don't affect the topological nature of the system, they are not able to alter the nature of the dispersion relation or the band gap dimensions. It is also interesting to observe that the second edge state, figure 2.12c, is less localized than the other, this can be explained considering that this is the state closer to the band gap edge; the distance from the bandgap edge is a factor that directly influences the energy localization.

Chapter 3

Topology based RF acoustic devices

3.1 Performed analyses in COMSOL

The main parameters that are going to be considered to study the behavior of the different topological devices are the S21 and the Y21 parameters. This are well know parameters in the electrical and microwave engineering. These parameters are fundamental to study the energy transmission in the device. The S21 parameter represents the forward transmission coefficient of a two-port network. It measures the ratio of the signal output at port 2 to the signal input at port 1, assuming all other ports are properly terminated, and it is expressed as the ratio between the the transmitted voltage at port 2 and the incident voltage at port 1 $S_{21} = \frac{V_2^-}{V_1^+}$. The Y21 parameter is part of the Y-parameter matrix and represents the forward transfer admittance of a two-port network, and it is mathematically expressed as $Y_{21} = \frac{I_2}{V1}|_{V_2=0}$. Also the also all the simulations have been done by setting a quality factor Q of 500. This quality factor is in agreement with the one obtained in the real device measurements. The quality factor is the ratio between stored energy and dissipated energy $Q = 2\pi \frac{E_{stored}}{E_{dissipated}}$, and gives us an idea of the localization of the energy. To obtain all these parameters, the COMSOL software has been employed. Every device was equipped with two electrodes, one for emitting the signal and a second one to receive it, and a ground. In particular, all electrodes were made of aluminum, while ground was simulated through a platinum layer on the bottom of the device. The anchors were simulated by imposing perfectly matched layers (PML) combined with low reflecting boundary conditions,

3.2 Introduction to a elliptical rods forest system

As showed in section 2.2, topological states can be generated in a forest of elliptical rods.

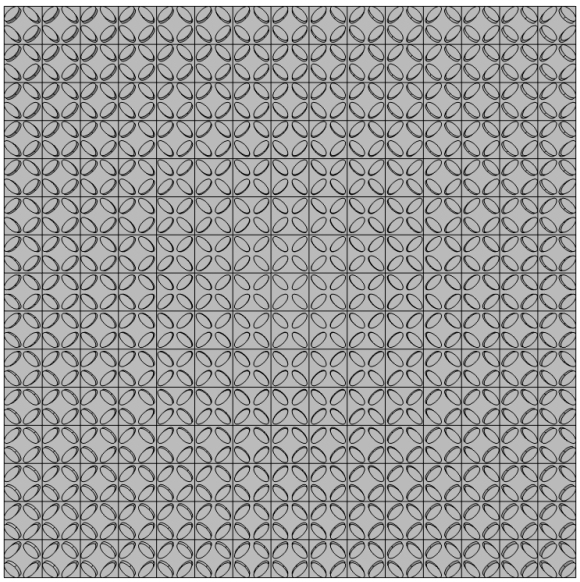

Figure 3.1: supercell 4 corners

In figure 3.1 is shown a supercell composed of a central array of normal insulators surrounded by topological insulators. In this way 4 edge states and 4 corner states will be created. The main focus in this section will be on the corner states, because of their higher energy localization and Q factor. When an out-of-plane harmonic perturbation is applied with a frequency that falls inside the dispersion relation band gap, no acoustic wave should propagate in the system. The presence of corner and edge states inside the bandgap leads to a spatially localized wave.

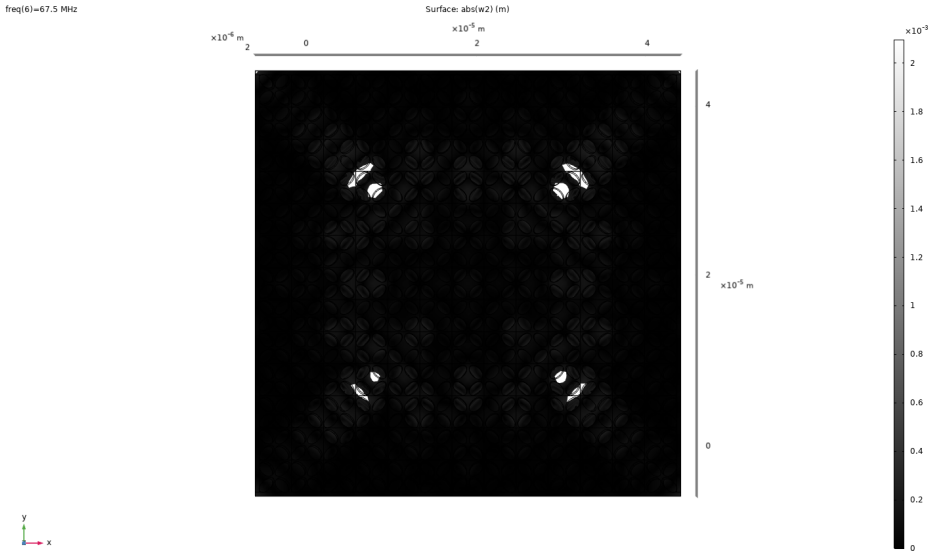

Figure 3.2: Corner states displacement in the supercell

In figure 3.2 is depicted the out-of-plane displacement when an harmonic perturbation is applied at the corner states frequency. Can be easily observed how the displacement is highly localized at the 4 corners of the interface between normal and topological insulators.

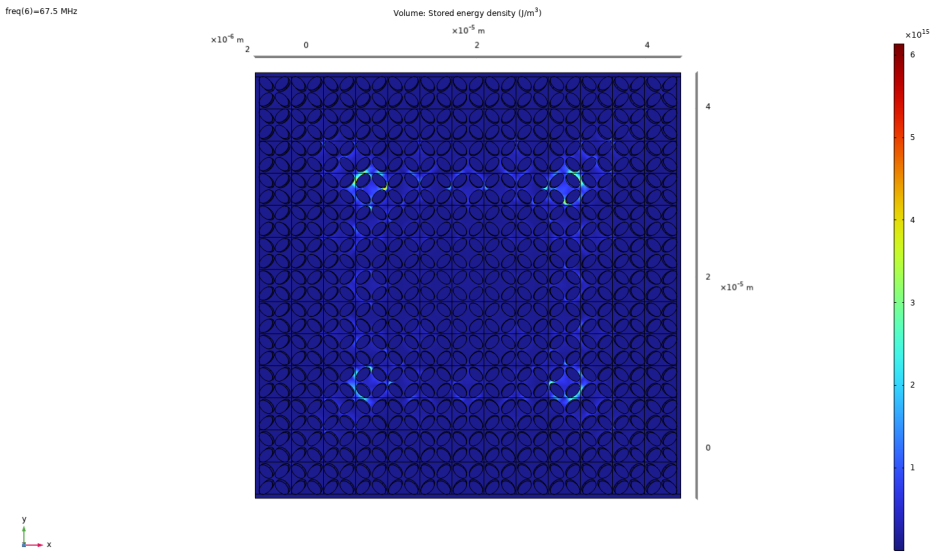

Figure 3.3: Corner states energy density in the supercell

The same considerations are valid for the energy density distribution, and this is clearly shown in figure 3.3.

3.3 Electrical driving of a elliptical rods forest supercell

Here it is important to remind that the substrate is a piezoelectric material with, underneath, a 80 nm thick layer of platinum used as ground. Thanks to the AlScN electromechanical coupling properties, it's possible to excite an acoustic wave by driving some electrodes on top of the surface and, more importantly, it's possible to obtain an electrical readout from the acoustic waves, similarly to a SAW. In this way the measurement of the S21 and S11 parameters can be an effective and easy way to measure the presence of topological states in real devices.

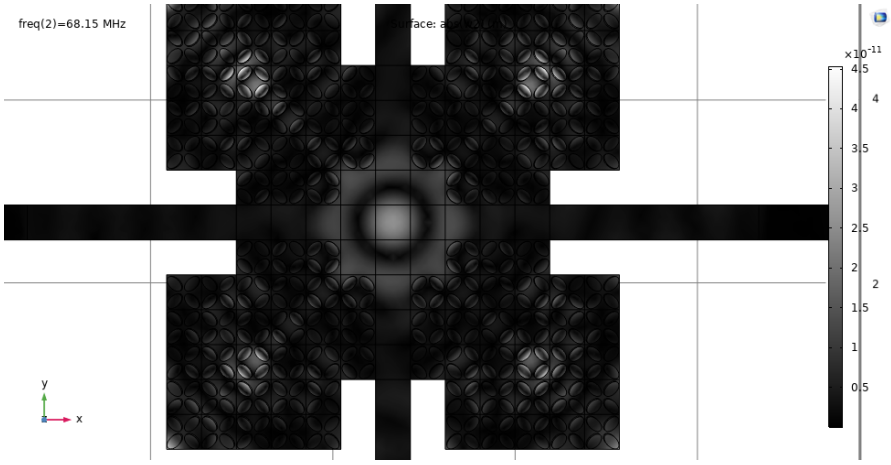

(a) Here is shown a device in which 4 identical corner states are excited through a central electrode

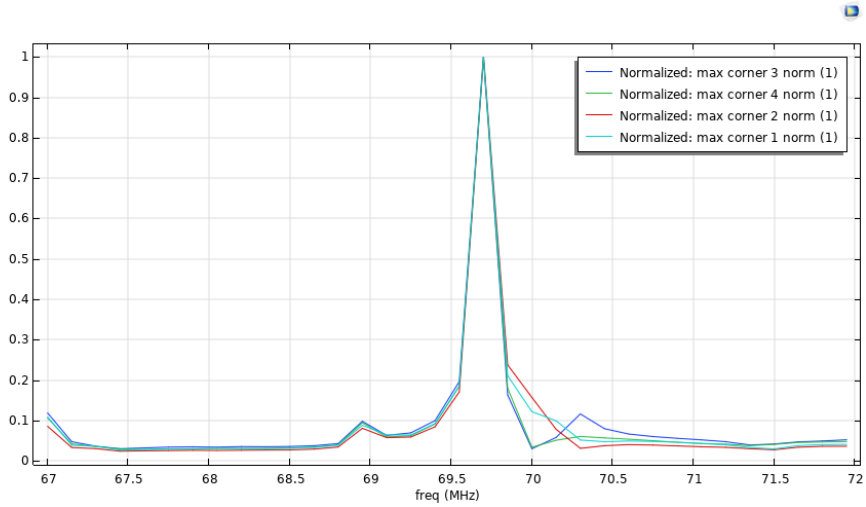

(b) Here is shown the displacement as a function of the frequency, is clear that the only considerable displacement takes place at the corner states frequency

Figure 3.4: Displacement for an acoustic piezoelectric device based on corner states technology

In figure 3.4a a structure having a central top electrode made of a 80 nm thick layer of Alluminum is presented. In figure 3.4a the resulting displacement outside the plane can be observed when the top electrode is driven at the corner states frequency. The structure also presents 4 anchors. It is interesting to notice that, the energy being localized in a small region around the corners of the interface between normal and topological insulators, the presence of anchors does not significantly affect the corner states. It's also important to see that in the frequency range

spanning the band gap, the corner state frequency is almost the only frequency at which there is a considerable displacement. This is quite clear from figure 3.4b, in which the normalized out of plane displacement is reported; as expected the only peak is the one at the corner state frequency.

3.4 Boundary effects on topological states

As already stated, the topological states have an intrinsic robustness towards defects. This stability is due to the fact that, the presence of single and isolated defects doesn't really affect the periodicity of the system, will not change the topological index of the cells, and consequently, will not affect the topological states. On the other hand, topological states are impacted by boundary conditions. Boundary conditions won't affect neither band gap nor the topological indexes but change the conditions at the edge of the Brillouin Zone. This effect leads to a change in the topological modes shape for edge states and a frequency shift for corner states (which are a flat line in the dispersion relation, so the only way they can adapt to a boundary condition variation is by shifting their frequency).

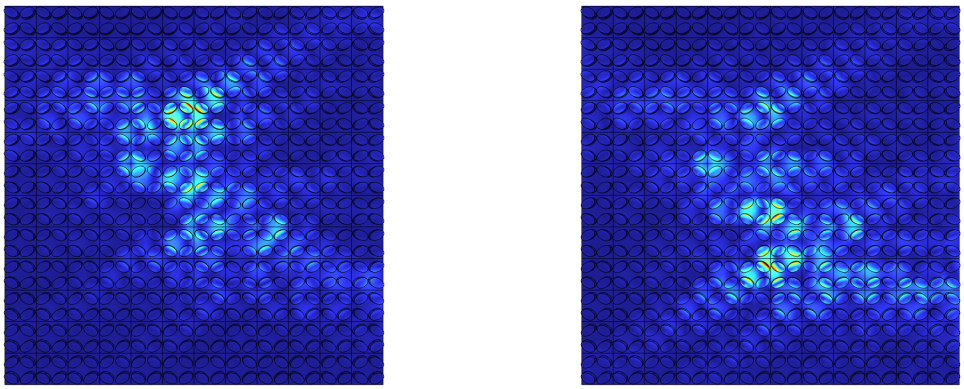

(a) 4 corners central electrode device **(b)** 4 corners central electrode device

Figure 3.5: Here is shown a comparison between two corner stetes at the same interface but with different boundary conditions. As can be observed the 2 corners have different frequency, this is due to the different boundary conditions

The boundary conditions can be changed in many different ways. For example, by applying a stress.The alteration of the boundary conditions can be also done by changing geometrical and topological aspects of the structure. This last possibility can be observed in figure 3.5, where it is shown a structure presenting two different

corners at the interface between NI and HOTI. Looking closely at the two different corners, can be noticed that the upper corner is mainly influenced by NI, while the lower corner is influenced more by HOTI. This difference causes a shift in the corner state frequency. Although being small, the shift can be observed in both frequency studies and eigenfrequency studies; this proves that the two corner states have different frequencies.

3.5 Edge corner coupling

Edge states and corner states are not isolated systems. It is possible to couple an edge state with a corner state.

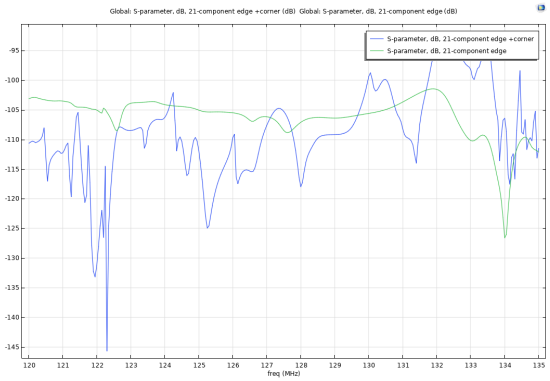

(a) Comparison between S21 parameters of the isolated edge state compared to the S21 of the edge state coupled to a corner state

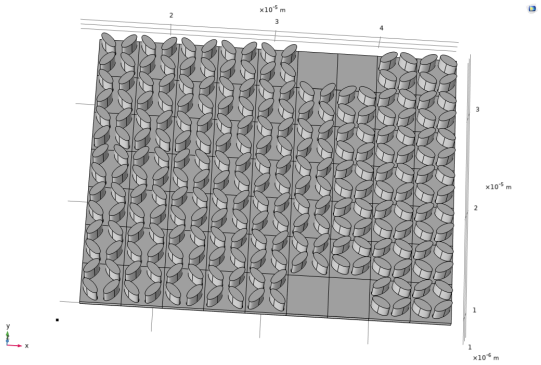

(b) Geometry of the corner-edge coupled device

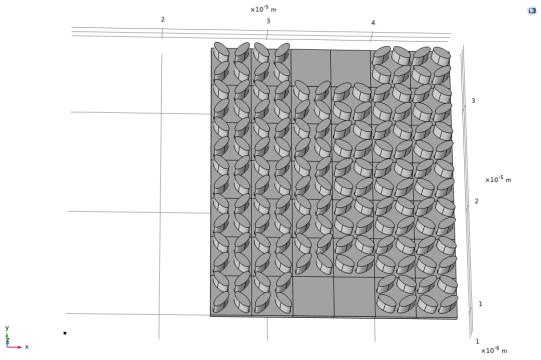

(c) Geometry of the edge state device without any corner in the vicinity

Figure 3.6: Comparison between the isolated edge and the corner-edge coupled system

This phenomena could be observed by looking at the S21 parameters of the

two different systems depicted in figure 3.6.The structure is built by depositing $2\mu m$ silicon rods on top of a $500nm$ AlScN substrate; each single is a square with $3.8\mu m$ edges and the axis of the elliptical rodes are respectively $b_1 = 0.9\mu m$ and $b_2 = 0.4\mu m$; the rotation angels that have been employed are respectively $\theta_{NI} = 45°$ and $\theta_{TI} = -45°$. It can be observed in figure 3.6a that, when the structure presents both the edge state and the corner state, at the corner state frequency the corner state is "activated" and captures the energy from the edge state causing a notch in the transmission. This coupling is possible only if the distance between the edge and the corner is not too large, otherwise the two topological states would behave as isolated systems.

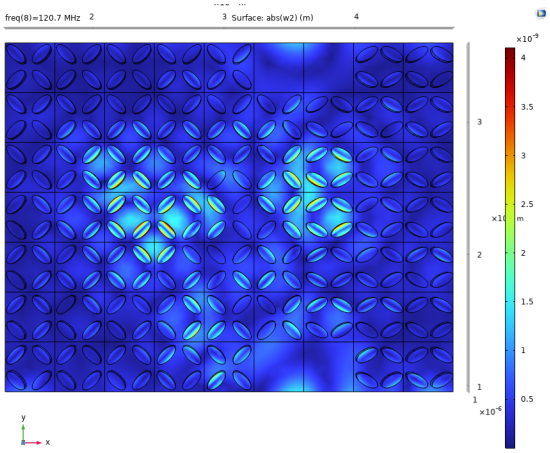

(a) Displacement map for a corner-edge coupled system

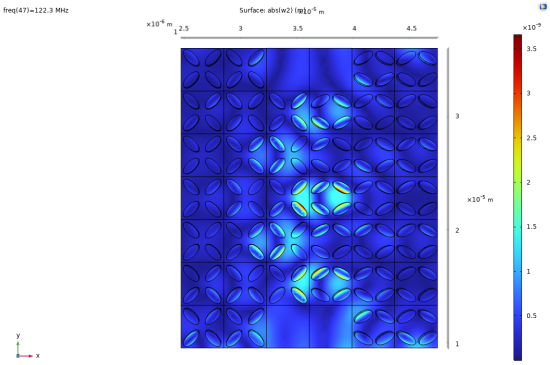

(b) Displacement map for the isolated edge state

Figure 3.7: Here it is reported a comparison between the field displacement of a edge-corner coupled system and a isolated edge structure

The mechanical coupling between these two modes is also visible by comparing the displacement of the two structures at the notch frequency, which is shown in figure 3.7. This can be observed in figure 3.7a where can be seen how the corner is excited by trapping the mechanical energy that was previously flowing in the edge state.

3.6 SSH system introduction

As mentioned in section 2.3, another interesting type of geometry for acoustic topological states is the SSH-type structure. The main goal of this section is to show how electrically driven RF devices can be obtained by the unit cell and the super-cells considered in section 2.3. In this type of structure, the generated edge state is used in a opposite way compared to the one in the elliptical rods forest treated in the previous paragraph. If in the elliptical rods, the edge was used as a channel to allow the flow of mechanical energy in a certain range of frequencies along the edge itself, in the SSH type structure the edge state is used to transmit the signal in a direction perpendicular to the wave propagation direction. This different approach leads to major differences in the signal response. In the SSH case the signal isn't driven by the chirality of the edge (which allows a flux along the longitudinal edge direction). If in the elliptical rods cell the edge state showed almost a flat line as S21 parameter, here the edge state behaves more like a corner state, it creates a region where the mechanical energy will localize. In this way the edge state will correspond to a peak in the S21 parameter. That's why in this circumstances the receiver can't be too far from the edge, otherwise it won't be able to interact with the localized energy and there will be no output signal from the device, as if there was no topological state at all.

3.7 SSH single edge RF device

The simplest device that can be obtained through this type of structure is a supercell with two top electrodes, figure 3.8, one used as driver and the other as signal-receiver, and a bottom electrode used as ground. To obtain these types of device, two $80nm$ thick and $3\mu m$ wide aluminum electrodes have been deposited on the AlScN bulk. The bottom electrode, instead, is obtained by depositing $80nm$ thick Platinum layer on the lower face of the AlScN film. In particular the left Al electrode has been used as driver and the right Al electrode as a receiver.

The structure depicted in figure 3.8 has been studied through FEM simulations in the frequency regime (using the piezoelectric module of COMSOL multiphysics). Different geometrical parameters have been tested and the structure has been finely tuned. The final single cell consists in a $500nm$ thick and $24\mu m$ wide layer of

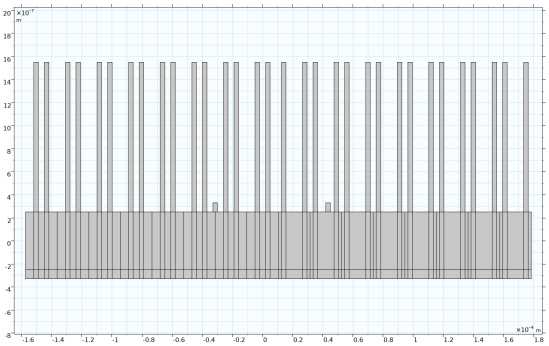

Figure 3.8: SSH supercell with two Alluminum electrodes

AlScN, with $2\mu m$ thick and $3\mu m$ wide SiO_2 rods. The supercell analyses has been performed by driving the right Al electrode with a 1W power. From this analyses the displacement, the energy density and the S21 parameters has been extracted.

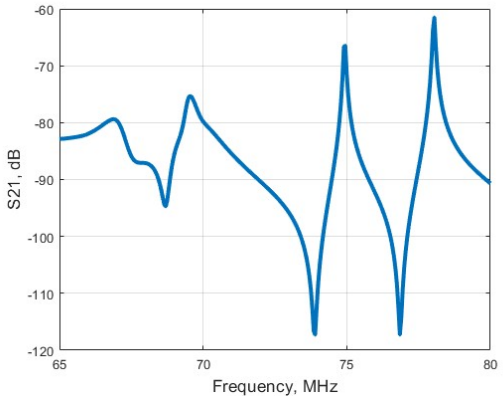

Figure 3.9: SSH supercell's S21 parameter

In this device the S21 parameter is a valuable and easy way of detecting the topological state presence. To confirm even more the energy and displacement localization this device was measured through an LDV system, which confirmed the high energy localization. By looking at the S21 parameters in figure 3.9 two peaks can be noticed, one for each edge state mode. The two peaks are separated by a deep notch. This notch is due to a phenomenon called Fano resonance. At the notch frequency the two states interact destructively creating the deep notch. This notch has an extremely high Q-factor (in the order of 10^5 as explained in [8]), which makes it suitable for sensing applications.

3.8 SSH rainbow trapping

3.8.1 Multiple sensors for noise averaging

When any type of sensing is performed, a way to reduce the noise could be taking simultaneous measurements with identical sensors. In this way, theoretically, the noise will be reduced by a factor $\sqrt{N}$ where N is the number of sensors employed. This reduction is simply due to a sort of compensation of the noise between the different measurements. This multiple sensors analysis can be effectively integrated into a single device by performing rainbow trapping. The rainbow trapping is a phenomenon that allows to localize waves at different frequencies in different spatial regions. This phenomenon can be obtained directly by concatenating SSH supercell with edge states at different frequencies in a single device.

3.8.2 Rainbow trapping structure

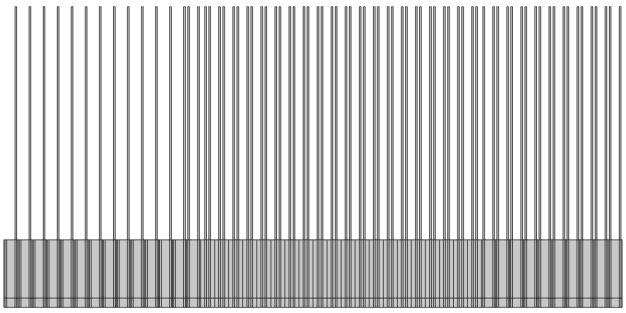

Figure 3.10: System built by concatenating two different SSH supercells

The different SSH supercells have to be carefully designed. The goal is to design a device that can be easily produced through lithographic steps, to do so, the thickness of the different materials have to be constant in the entire device (building a device with different rod thicknesses would require a complex manufacturing process). The starting point is a SSH supercell having 2 μm thick rods deposited on top of 500nm AlScN bulk. To shift the working frequency, while keeping the thicknesses constant, a tuning of the width of both the single cell and the rods

was performed. In the every single cell, the width modification was done while maintaining constant the distance between the rods and between rods and edges. So, by considering a factor N_{scale} for a specific supercell in the rainbow trapping system, the rods width in the supercell will be $w_{rod} = w_0 N_{scale}$, where w_0 is the non scaled rod width (in our case $3\mu m$) while, to keep the the rod-rod and the rod-edge distances constant over the whole device, the cell width, for every supercell, is enlarged by a quantity $2(w_{rod} - w_0)$. In this way a structure such as the one in figure 3.10 is obtained, where the periodicity is not perturbed along the entire device.

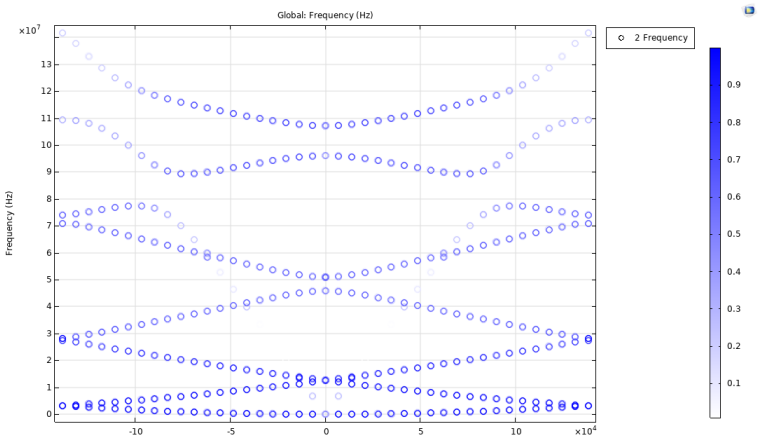

(a) Dispersion relation for a cell with 0.7 scaling factor

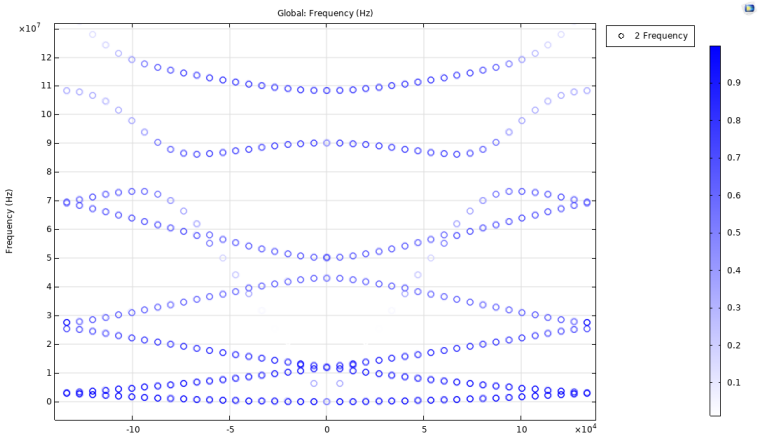

(b) Dispersion relation for a cell with 0.9 scaling factor

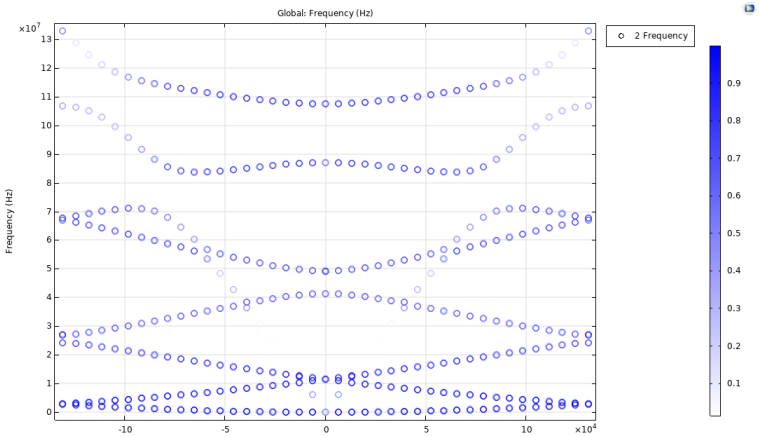

(c) Dispersion relation for a cell with 1 scaling factor

Figure 3.11: Dispersion relation for the single cells scaled as explained in the paragraph

The previously described tuning is quite effective. This is confirmed by the dispersion relations in figure 3.11, where it can be observed that by performing this sort of scaling the dispersion relation is almost rigidly and linearly shifted.

3.8.3 Two edges rainbow trapping device

The first rainbow trapping device that is going to be discussed is a two topological edges device. This device is made up of two SSH supercells. Each supercell contains 14 unit cells, 7 normal insulators and 7 topological insulators. The single unit cell is the one described in Section 2.4

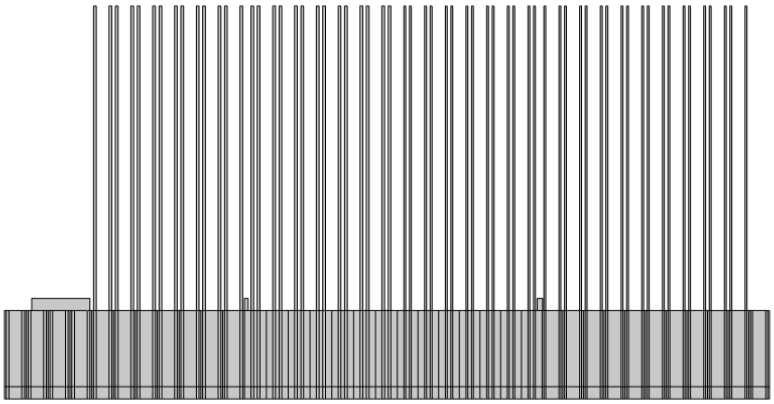

Figure 3.12: Two edges rainbow trapping device

The device geometry is illustrated in figure 3.12. As can be seen, the structure has a larger electrode on the left side, which will be used as driving electrode. This electrode will induce an acoustic wave that will propagate across the device and, thanks to the piezoelectric bulk, will generate an electric signal. Smaller electrodes are located exactly where the interface state is going to appear. These last electrodes position has been chosen to maximize the electromechanical coupling between electrodes and topological states (which is going to be the maximum displacement region). The first SSH supercell has the same dimension as the system in section 2.4.3, the second, on the other hand, has been scaled (in the previously illustrated way) by a factor 0.7.

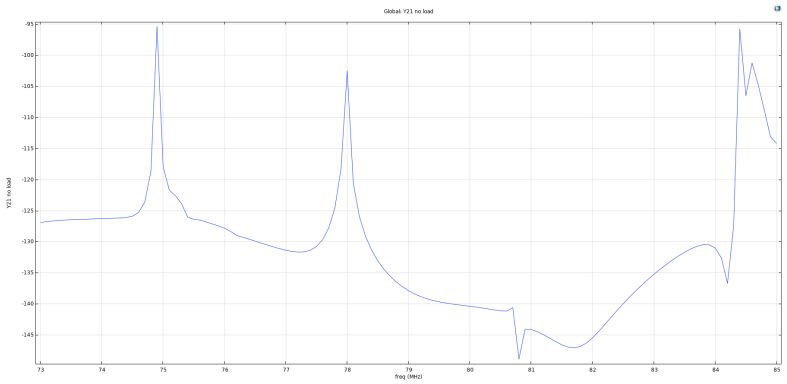

Figure 3.13: Two edges Y21

This scaling has been carefully designed to align the topological state of the second SSH with the end of the bandgap of the first SSH supercell. In this way, once the frequency fells into the bandgap of the first supercell, no signal will be detected by the receivers until the first topological state frequency is reached. At this first frequency, a spike in transmission will appear. The second spike in figure 3.13 corresponds to the second topological state of the first supercell. After this second spike no signal will be transmitted. This is due to the fact that, even if thee device is operating in the first supercell bandgap. This situation will remain unchanged until the first topological state frequency of the second supercell. This frequency has been located at the band edge of the first supercell. In this way the signal can cross the first SSH region. After crossing the first supercell spatial region, the signal reaches the second SSH. At this point the first topological state of the second supercell is triggered. At this frequency the output signal will have both a component from the first receiver (which is crossed by the wave that propagates to the second topological edge) and from the second receiver that will capture the signal from the topological state localized displacement. The overall output signal is going to be dominated by the topological state component. This is due to the high amount of localized energy. This is quite clear in figure 3.13, where the three peeks correspond in sequence to the two topological states of the first supercell and the first topological state of the second supercell.

3.8.4 Three edges rainbow trapping device

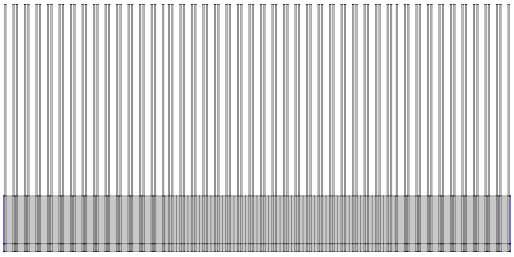

Figure 3.14: Geometry for the 3 edges rainbow trapping device

The two edges device can be extended to three edges quite directly, obtaining the device in figure 3.14. The major difference here is the tuning. The major issue is that, in order to observe the last topological transmission peak, the last receiver signal has to overcome the signal coming from the propagating wave that crosses the previous 2 receivers. In order to mitigate this problem, the tuning has to be performed even more carefully than before. The supercells in the final structure have scale factors of: 1.35, 1 and 0.68.

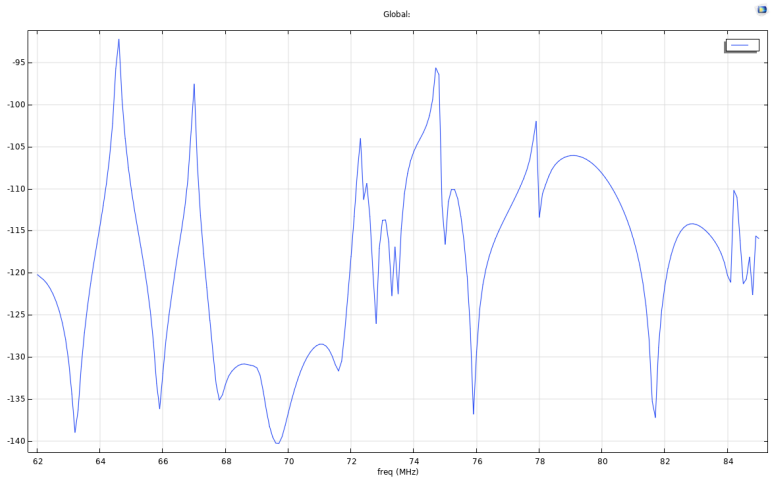

Figure 3.15: Y21 3 edges

With this scaling factors the peaks of every edge state are perfectly visible in the Y21 plot in figure 3.15, although the peak of the last supercell is considerably smaller than the others.

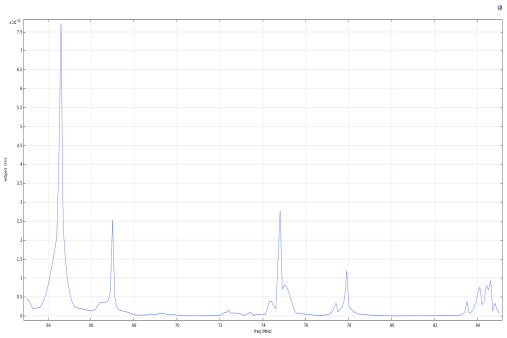

(a) The graph represents de out of plane displacement for a 3-edges SSH device

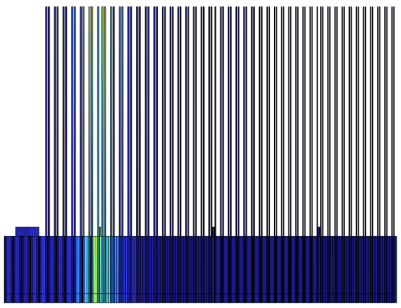

(b) Edge mode of the first edge state at 67.1 MHz

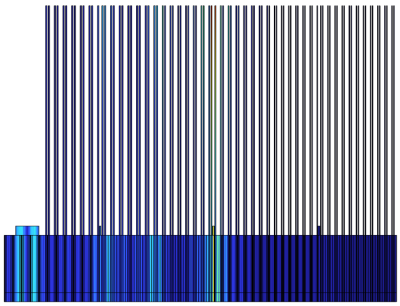

(c) Edge mode of the second edge state at 74.7 MHz

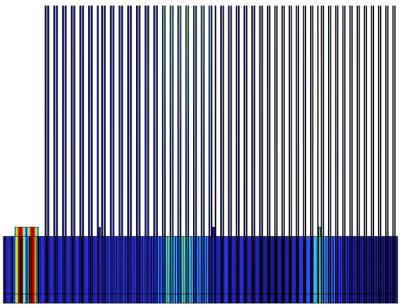

(d) Edge mode of the third edge state at 84MHz

Figure 3.16: The pictures show the displacement at different frequencies, the peeks in figure 3.16d correspond to the edge state, in the other figures are shown snapshots of the localized edge modes for the three edge states

The displacement follows, as expected, the Y21 behavior; presenting peaks at the topological states frequencies, as can be seen in figure 3.16.

3.8.5 Example of sensing application

In this subsection is going to be discussed a possible application of these devices. As it was already explained in section 3.4 topological modes are almost defects insensitive but can be affected by changes in the boundary conditions or in the structure parameters(such as geometrical dimensions, Young modulus, density...). In this way the topological states can be effectively used for sensing purposes. Here is going to be analyzed a rainbow trapping accelerometer.

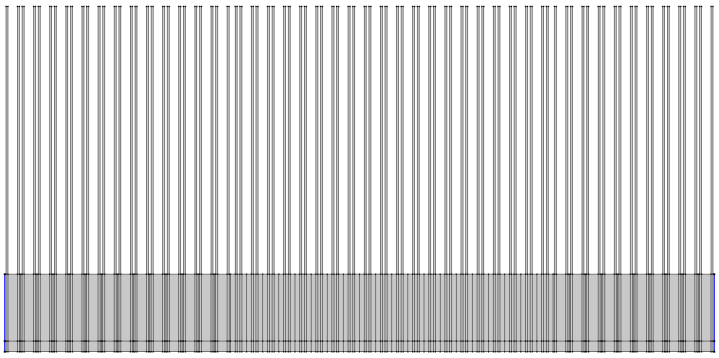

Figure 3.17: Rainbow trapping device with fixed boundary conditions at the highlighted edges

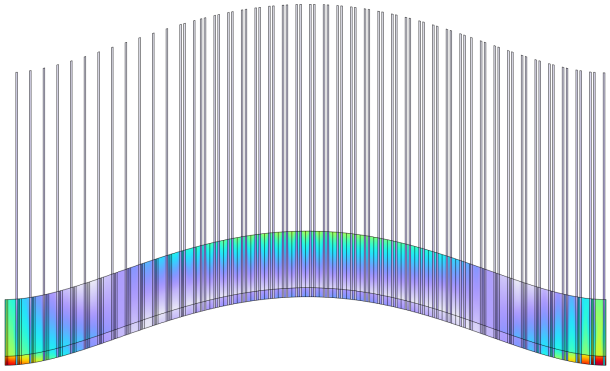

Figure 3.18: Stress distribution in the device when a a vertical acceleration is applied

The device is structured as the previously discussed two topological edges rainbow trapping device. To study the device response to accelerations, fixed boundary conditions have been imposed over the left and right edge, as it is shown in figure 3.17. In this way the simulation is taking into account the presence of anchors that will limit the displacement at the two extremities of the device. The study was performed in two steps, first the acceleration was applied using a stationary study. This was based on the assumption that the force was applied to the device for a long enough time interval to allow the device to reach a stationary condition. The second step consisted in performing a frequency study similar to the ones done in the previous sections to obtain the S21 and the Y21 parameters. As expected, when a force is applied, the modes are modified. Looking at the Y21 parameters, two effects can be observed: a frequency shift and a change of the transmission peaks height. The first one can be re-conduced to two main causes.

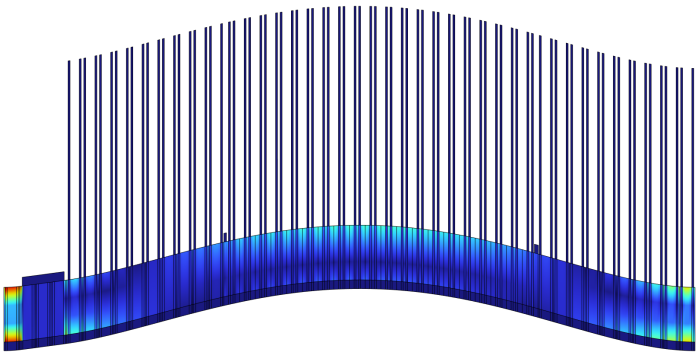

Figure 3.19: Charge distribution in the device when a a vertical acceleration is applied

First of all, the stress leads to a charge accumulation in the piezoelectric material, but, due to the ground and electrodes presence, a charge discontinuity appears. This charge discontinuity directly affects the wave propagation velocity causing a frequency shift. The second effect comes from the fact that the topological states perceive the stress change in the device boundary conditions, and consequently, the edge mode shape changes, leading to a frequency shift. While the topological states are shifted, the band gap is not modified by any means by the applied stress, which is not changing any topological parameter. So the edge states can move towards the center of the band gap or towards the closes band gap edge. Is fundamental to remind that the states localization is directly related to how far the edge state is from the band gap edge. The more the edge state is close to the band gap center, the more the localization is going to be higher. The localization plays a major role in determining how much energy is going to be captured by the receivers, and therefore, how big the transmission peaks are going to be. The second main effect on the transmission peak height is due to the fact that, when a high acceleration is applied, the device is deformed. This deformation causes a perturbation in the periodicity of the structure that can disturb the topological state and more importantly slightly reduce the bandgap dimension. This reduction leads to a lower localization and so a reduction of the transmission peaks. Even though the change in the power of the output signal is observable, the main effect, even at considerable accelerations (thousands of g), remains the frequency shift.

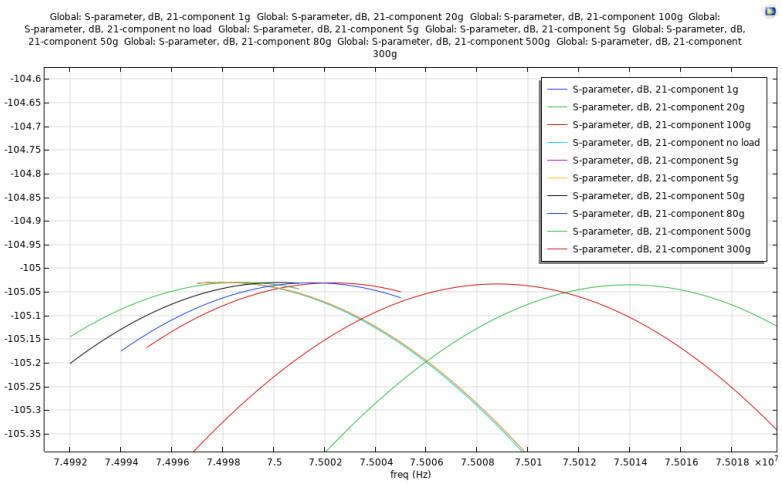

Figure 3.20: Shift with different accelerations of the Y21 peak corresponding to the first edge state of the first supercell, f=75MHz

From figure 3.20, can be seen how the Y21 of the peak at 75 MHz shifts when different accelerations are applied. From this dataset, the device response has been calculated considering how the current output varies when an acceleration is applied.

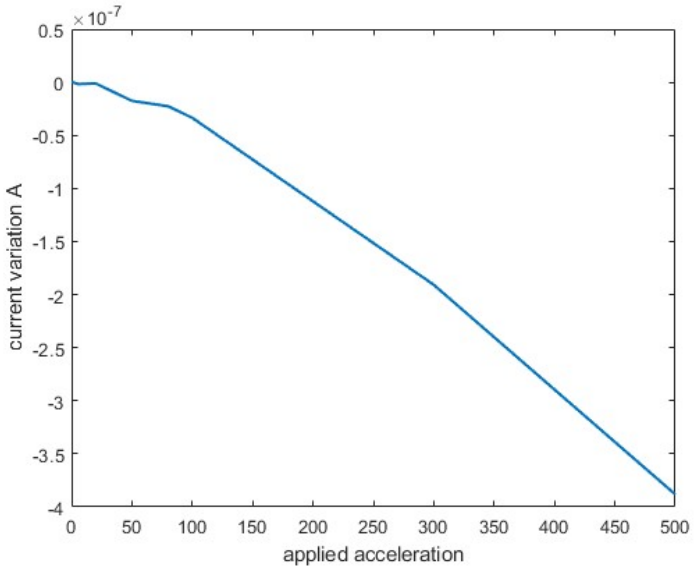

Figure 3.21: Trend of the output current variation with respect to the applied acceleration

By looking at the device current variation, in figure 3.21, can be noticed that

the device has a good linearity over a broad range of accelerations. The next step was to extract the limit of detection (LOD). To do so, it was assumed that the main noise component was coming from the thermo-mechanical noise. The thermo mechanical noise comes from the self-heating of the device due to its vibration. This is a reasonable assumption and was confirmed by studies at cryo temperature of the SSH device presented in section 2.3.4. During those analyses both quality factor and responsivity of the device greatly improved at cryogenic temperatures. The limit of detection was calculated for the peak at 74.997 MHz (where all the acceleration and stress simulations have been done) by considering an input power $P_{in} = 1W$. The corresponding bandwidth was B_w=0.082 MHz. The frequency uncertainty due to thermo mechanical noise can be obtained through the formula $\Delta f_{th-mech} = \sqrt{\frac{K_b T B_w}{4 P_i n}} \frac{f_0}{Q}$. Where f_0 is the resonant frequency. For this device the thermo-mechanical noise was$\Delta f_{th-mech} = 2.5 mHz$. By considering the thermo-mechanical noise and the device response, the limit of detection was equal to $LOD = 15 \mu g$. This result could be easily improved with a deeper study of the electrodes geometry and the device dimensions. Maximizing the electrodes dimensions should lead to a larger charge discontinuity and consequently a larger frequency shift in the peaks, while tuning the dimensions of the device should lead to a more effective response with respect to the acceleration, in practice there would be a larger deformation and larger stress at the boundaries which would directly cause a larger shift in the topological modes frequency.

Conclusions

The RF topological Micro-Electro-Mechanical Systems discussed in this thesis are promising in many different fields. The combination of versatility, efficiency and straightforward manufacturing process, justify the growing interest that they are arousing. The goal of this thesis is to provide the basic knowledge to understand and use this topological phenomena and to design some possible electro-mechanical devices based on this effects. Some, here presented, key factors for the study of these devices are: the ability to relate topological effects and geometry in the devices; the quantum physics knowledge of the topological mechanism behind this phenomena; how to obtain an electrical readout of the topological localized states. Another fundamental aspect it's the tunability of these devices, this tunability is easily obtainable through lithographic processes. Another interesting aspect is the scalability. It would be possible to obtain this devices of few microns, the only limit it's the lithographic process itself. This last aspect is surprising, considered that devices with this dimensions usually operates in the GHz range of frequencies. This study also shows a possible way of studying this type of devices based on S21 parameters, Y21 parameters, displacement, anergy density and dispersion relations. All parameters that can be obtained through a simple FEM simulation. It's also worth to notice how easily this devices can be used for sensing applications thanks to their dependence on the boundary conditions while remaining robust against defects (making the manufacturability even easier). It's still plenty of possible applications that are still worth to investigate. Temperature sensing, IR sensing and stress sensing are just few possible example. Devices based on topology could pave the way not only to new RF sensing systems but towards a completely new way of building acoustic systems and MEMS.

Appendix A

MATLAB code for ZAK phase and Chern number evaluation

```
%% Function chern

function [chern_number,Int_mode]=chern_calculation(u_disp,BZ_sampling
    ,nx,deltax,ny)
Int_mode=zeros(1,BZ_sampling);
chern_number=0;


fac=1/2/3700/6000^2;


for j=1:BZ_sampling %for used for integrating over Bz

 for n=1:nx            %integral over x
 %for l=1:ny    %integral over y
 l=1;
if j<BZ_sampling
  %  Int_mode1=(conj(u_disp(l,n,i+j))*u_disp(l,n,j)-abs(u_disp(l,n,j)
    ))*deltax/(2*pi/BZ_sampling);  %integrate the mode over x, the
    gradient has been decomposed considering deltax

Int_mode1=dot(conj(u_disp(l,n,j)),u_disp(l,n,j+1));
end

if j==BZ_sampling
```

```
23 Int_mode1=dot(conj(u_disp(l,n,j)), u_disp(1,n,1)*exp(-1i*2*pi/(deltax
       *nx)*(n-1)*(deltax*nx)/(nx-1))) ;
24
25 end
26 Int_mode(1,j)=Int_mode(1,j)+Int_mode1;
27
28 % end
29
30  end
31
32
33 chern1=log(Int_mode(1,j));
34
35 chern_number=chern_number+chern1;
36 end
37 chern_number=-imag(chern_number);
38 % chern_number=mod(chern_number,(2*pi));
39
40 end
```

Bibliography

Bibliography

[1] M. Carrara et al. «Metamaterial-inspired structures and concepts for elastoacoustic wave energy harvesting». In: *Smart Materials and Structures* 22 (2013), p. 065004.

[2] Pegah Azizi et al. «Dynamics of Self-Dual Kagome Metamaterials and the Emergence of Fragile Topology». In: *Physical Review B* (2023).

[3] Wladimir A. Benalcazar, B. Andrei Bernevig, and Taylor L. Hughes. «Quantized electric multipole insulators». In: *Science* (2017).

[4] Christian Bengs. «Theory and Calculation of Abelian and Non-Abelian Geometric Phase Factors with Spin Dynamica». In: *Journal of Magnetic Resonance* (2023).

[5] M. V. Berry. «Quantal phase factors accompanying adiabatic changes». In: *Proceedings of the Royal Society of London. Series A, Mathematical and Physical Sciences* 392 (1984), pp. 45–57. DOI: 10.1098/rspa.1984.0023.

[6] Severin Bunk and Richard J. Szabo. «Topological Insulators and the Kane-Mele Invariant: Obstruction and Localisation Theory». In: *arXiv preprint* (2019).

[7] Anna Dalklinta et al. «Tunable phononic bandgap materials designed via topology optimization». In: *Journal of the Mechanics and Physics of Solids* (2018). URL: www.elsevier.com/locate/jmps.

[8] Jacopo M. De Ponti et al. «Localized Topological States Beyond Fano Resonances via Counter-Propagating Wave Mode Conversion in Piezoelectric Microelectromechanical Devices». In: *Journal Name* (2024). Received: 22 June 2024; Accepted: 28 October 2024. DOI: 1234567890.

[9] Pierre A. Deymier. *Acoustic Metamaterials and Phononic Crystals*. Springer, 2013.

[10] Liang Fu and C. L. Kane. «Time reversal polarization and a Z_2 adiabatic spin pump». In: *Physical Review B* 74 (19 Nov. 2006). Received 13 June 2006; revised manuscript received 12 September 2006; published 8 November 2006, p. 195312. DOI: 10.1103/PhysRevB.74.195312. URL: https://link.aps.org/doi/10.1103/PhysRevB.74.195312.

[11] Liang Fu and C. L. Kane. «Topological insulators with inversion symmetry». In: *Physical Review B* (2007).

[12] Hidenori Fukaya et al. «TKNN formula for general Hamiltonian». In: *arXiv preprint* (Mar. 2020). arXiv: arXiv:1903.11852 [hep-th].

[13] M.Z. Hasan and C.L. Kane. «Topological Insulators». In: *Reviews of Modern Physics* 82 (2010), pp. 3045–3067.

[14] Mahmoud I. Hussein, Michael J. Leamy, and Massimo Ruzzene. «Dynamics of Phononic Materials and Structures: Historical Origins, Recent Progress, and Future Outlook». In: *Journal of Applied Mechanics* (2019).

[15] C. L. Kane and E. J. Mele. «Quantum Spin Hall Effect in Graphene». In: *Physical Review Letters* (2005).

[16] W. Kohn. «Analytic Properties of Bloch Waves and Wannier Functions». In: *Physical Review* (1959).

[17] Srijata Lahiri and Saurabh Basu. «Wannier charge center, spin resolved bulk polarization, and corner modes in a strained quantum spin Hall insulator». In: *Physical Review B* (Mar. 2024).

[18] Jekwan Lee et al. «Spinful hinge states in the higher-order topological insulators WTe». In: *Nature Communications* 14 (2023). DOI: 10.1038/s41467-023-37482-0.

[19] Guancong Ma, Che Ting Chan, and Meng Xiao. «Topological phases in acoustic and mechanical systems». In: *Nature Reviews Physics* (2019).

[20] Tommaso Maggioli. «Investigation of Elastic Topological Protected Interface Modes on RF Piezo-Electric MEMS Technology». MA thesis. Politecnico di Torino, 2020.

[21] Julio Andrés Iglesias Martínez et al. «Topological waves guided by a glide-reflection symmetric crystal interface». In: *Physical Review B* 106.6 (2022), p. 064304. DOI: 10.1103/PhysRevB.106.064304.

[22] Topological Condensed Matter. *The Haldane Model*. URL: https://topocondmat.org/w4_haldane/haldane_model.html.

[23] John McGreevy. «Gapless Topological States: An Overview». In: *Annual Review of Condensed Matter Physics* (2020).

[24] Annika Ott and Svend-Age Biehs. «Topological near-field heat flow in a honeycomb lattice». In: *International Journal of Heat and Mass Transfer* (2023). URL: https://www.elsevier.com/locate/hmt.

[25] Raj Kumar Pal et al. «Amplitude-dependent topological edge states in nonlinear phononic lattices». In: *Physical Review B* (Mar. 2018).

[26] Christopher W. Peterson et al. «A quantized microwave quadrupole insulator with topologically protected corner states». In: *Nature* (2018). DOI: 10.1038/nature25777.

[27] Jacopo M. De Ponti et al. «Tailored Topological Edge Waves via Chiral Hierarchical Metamaterials». In: *Physical Review Letters* (2023).

[28] Zohar Ringel and Yaacov E. Kraus. «Determining topological order from a local ground-state correlation function». In: *Physical Review B* (2012).

[29] Matheus I. N. Rosa et al. «Material vs. structure: Topological origins of band-gap truncation resonances in periodic structures». In: *Physical Review B* (Dec. 2023).

[30] Ashutosh Kumar Singh, S. D. Ramarao, and Sebastian C. Peter. «Rare-earth based half-Heusler topological quantum materials: A perspective». In: *APL Materials* 8.6 (2020), p. 060903. DOI: 10.1063/5.0006118.

[31] Alexey A. Soluyanov and David Vanderbilt. «Computing topological invariants without inversion symmetry». In: *Physical Review B* 83 (2011), p. 235401. DOI: 10.1103/PhysRevB.83.235401.

[32] Sebastian Stengele. *Berry's Phase*. Proseminar - Algebra, Topology, and Group Theory in Physics. 2018.

[33] D. J. Thouless et al. «Quantized Hall Conductance in a Two-Dimensional Periodic Potential». In: *Physical Review Letters* (1982).

[34] Hai-Xiao Wang, Guang-Yu Guo, and Jian-Hua Jiang. «Band topology in classical waves: Wilson-loop approach to topological numbers and fragile topology». In: *Nature Physics* (2019).

[35] Hai-Xiao Wang, Guang-Yu Guo, and Jian-Hua Jiang. «Band topology in classical waves: Wilson-loop approach to topological numbers and fragile topology». In: *Physics Letters* (2023). URL: https://example.com.

[36] Ying Wu et al. «On-chip higher-order topological micromechanical metamaterials». In: *Nature Communications* (2023).

[37] Meng Xiao et al. «Geometric phase and band inversion in periodic acoustic systems». In: *Nature Physics* (2015).

[38] Wang Yao, Di Xiao, and Qian Niu. «Valley-dependent optoelectronics from inversion symmetry breaking». In: *Physical Review B* (2008).

[39] S. Zhang et al. «A Novel Ultrathin Elevated Channel Low-temperature Poly-Si TFT». In: 20 (Nov. 1999), pp. 569–571.

[40] Changlong Zhu, Claudiu Genes, and Birgit Stiller. «Optoacoustic Entanglement in a Continuous Brillouin-Active Solid State System». In: *Physical Review Letters* (2024).